1967

Transport properties of thulium single crystals

Leon Roger Edwards
Iowa State University

EDWARDS, Leon Roger, 1940-
TRANSPORT PROPERTIES OF THULIUM SINGLE CRYSTALS.

Iowa State University, Ph.D., 1967
Physics, solid state

TRANSPORT PROPERTIES OF THULIUM SINGLE CRYSTALS

by

Leon Roger Edwards

A Dissertation Submitted to the

Graduate Faculty in Partial Fulfillment of

The Requirements for the Degree of

DOCTOR OF PHILOSOPHY

Major Subject: Experimental Physics

Approved:

Signature was redacted for privacy.

In Charge of Major Work

Signature was redacted for privacy.

Head of Major Department

Signature was redacted for privacy.

Dean of Graduate College

Iowa State University
Of Science and Technology
Ames, Iowa

1967

TABLE OF CONTENTS

I. INTRODUCTION

Thulium, atomic number 69, was discovered in 1879 by P. T. Cleve and named after Thule, the ancient name of Scandanavia. Thulium is a member of a family of elements called the Lanthanides or, more commonly, the rare earths. This series of elements begins with lanthanum, atomic number 57, and ends with lutetium, atomic number 71.

The conduction band of the rare earths except cerium, europium and ytterbium consists of three electrons -- nominally, one 5d and two 6s. This is why the rare earths behave the same chemically and are so difficult to separate from one another. Also, one would expect the transport properties such as the electrical resistivity, Seebeck coefficients and the thermal conductivity to be quite similar. However, experimentally the transport properties are very anomalous (1-7). This behavior is attributed to the influence of the incomplete 4f electron shell on the conduction electrons. Thulium has twelve 4f electrons of which two are unpaired. According to Hund's rules, the trivalent thulium ion has a $^3H_6$ ground state configuration.

Electrical resistivity measurements have been made on polycrystalline thulium from 1.3 to 300°K by Colvin et al. (7). A maximum in the resistivity at 54.5°K was interpreted as the Néel temperature.

Measurements of the Seebeck coefficients of polycrystalline thulium by Born et al. (8) exhibited a sharp maximum in the Seebeck coefficient at 55°K and no other anomalies. The sharp maximum was interpreted as the onset of antiferromagnetism.

Jolliffe et al. (9) have measured the thermal conductivity of

polycrystalline thulium at 291°K. They found a thermal conductivity of 0.140 (watt/cm-°K) and a Lorenz number of 3.45×10^{8} (volt/°K)^2. The thermal conductivity of polycrystalline thulium has been measured from 2 to 100°K by Aliev and Volkenshteĭn (10). An anomaly was found at 53°K and was interpreted as the Néel temperature.

The heat capacity of polycrystalline thulium has been measured between 15 and 260°K by Jennings et al. (11). A lambda anomaly was observed near 55°K which was associated with the onset of antiferromagnetic ordering. Thulium was found to have a Debye temperature of 167°K. Lounasmaa and Sundström (12) have measured the heat capacity of thulium between 3 and 25°K and have found no anomalies.

The magnetic moment of polycrystalline thulium has been measured at 4.2°K and from 20 to 300°K in applied fields of 3 to 18 kOe by Rhodes et al. (13). Antiferromagnetism was found to set in below 51°K and Curie-Weiss behavior was observed above 51°K. The effective number of Bohr magnetons, μ_{eff}, was found to be 7.6 in agreement with the theoretical value 7.56. The inverse susceptibility was extrapolated to the temperature axis to obtain a Curie temperature of 20°K. This Curie temperature is in good agreement with the 22°K as calculated by Néel (14,15). A tendency toward ferromagnetism was observed at 4.2°K. Davis and Bozorth (16) have measured the magnetic moment of polycrystalline thulium from 1.3 to 300°K in applied fields up to 12 kOe and have found a Néel temperature of 60°K and a Curie temperature of 22°K.

Jelinek et al. (17) have measured the A. C. susceptibility of polycrystalline thulium from 4.2 to 90°K in an applied field of 10 Oe. Maxima in the susceptibility curves were observed at 57.5 and 30°K. The maximum

at 57.5°K was interpreted as the Néel point.

Using a thulium single crystal Koehler et al. (18,19,20) have determined the magnetic structure by neutron diffraction measurements. Thulium was found to be a paramagnet above 56°K, a sinusoidally modulated antiferromagnet between 38 and 56°K, and a ferrimagnet below 38°K. All moments were found to lie along the hexagonal axis. These structures are illustrated in Figure 1.

Because of the magnetic and crystalline anisotropy of thulium, single crystal data are necessary for the understanding of its transport properties.

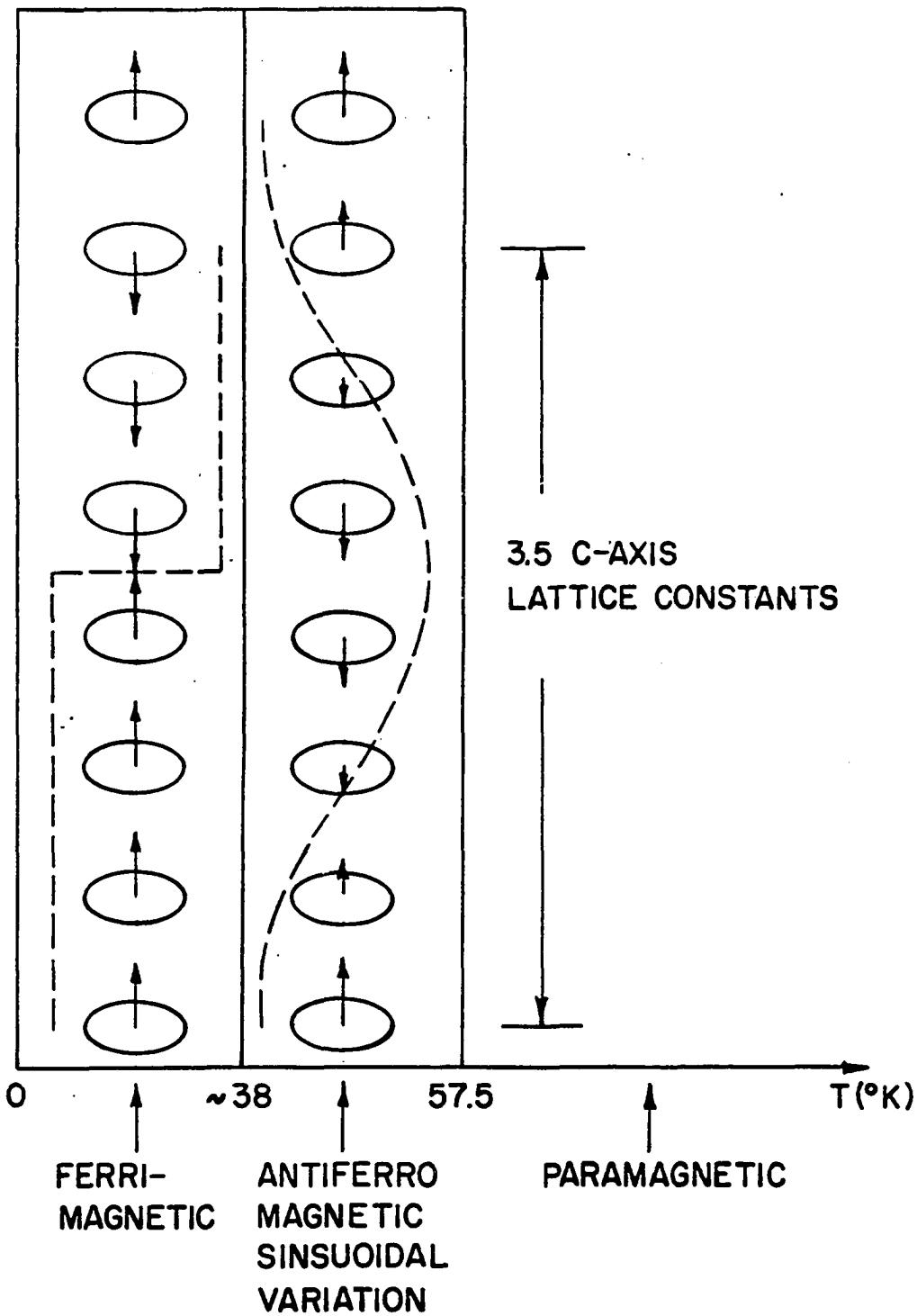

Figure 1. The ordered spin structure of thulium as observed by neutron diffraction (19).

II. REVIEW OF THEORY

A. Electrical Resistivity

The question, "What impedes the flow of electrons in a metallic lattice?", has been of interest for several decades. Houston (21) and Bloch (22) have shown that the wave vector of an electron does not change in the presence of a perfectly periodic potential, and thus a perfect lattice has zero resistivity. The electrical resistivity of a metal is caused by the scattering of electrons by lattice aperiodicities. In the rare earths the deviations from periodicity which scatter electrons are:

(1) defects (impurities, vacancies, dislocations and twins);

(2) thermal motion of the ions (phonon scattering); and

(3) thermal motion of the magnetic moments (magnon scattering).

These scattering processes are discussed in this order below.

Theoretically the electrical resistivity is treated in the framework of formal transport theory. A general description of this theory is given by Ziman (23,24). If the electronic scattering can be described by a relaxation time, then the electrical conductivity can be formally calculated from

$$\sigma_{ij} = (e^2/4\pi^3\hbar) \int_{E_F} \tau v_i \, d\mathcal{S}_j \quad , \tag{2.1}$$

where e is the electronic charge, $\hbar$ is Planck's constant divided by 2π, τ is the relaxation time, v_i is the i^{th} component of the electron velocity at the Fermi surface, and $d\mathcal{S}_j$ is an elementary area of the Fermi surface with normal in the j^{th} direction.

If the various electronic scattering processes are independent, then

the resistivity may be written

$$\rho = \rho_R + \rho_P \quad , \tag{2.2}$$

where ρ_R is the residual resistivity (resistivity due to defects) and ρ_P is the lattice resistivity (resistivity due to phonon scattering). This is known as Matthiessen's rule and its validity is discussed by Ziman (23, p.285). For a magnetic material the resistivity can be written

$$\rho = \rho_R + \rho_P + \rho_M \quad , \tag{2.3}$$

where ρ_M is the resistivity due to magnon scattering.

If the number of defects is small and the temperature is not too low, then ρ_R is, to a good approximation, independent of temperature.

The temperature dependence of ρ_P is described analytically by the Bloch-Grüneisen formula

$$\rho_P = A\ (T/\theta_D)^5\ J_5(\theta_D/T) \quad , \tag{2.4}$$

where A is a constant depending on Fermi surface parameters, θ_D is the Debye temperature, and J_5 belongs to the class of Debye integrals. A derivation of this formula is given by Ziman (23,p.357). In the limit $T \gg \theta_D$ J_5 behaves as $(\theta_D/T)^4$ so that

$$\rho_P \sim T \quad . \tag{2.5}$$

For the opposite limit $T \ll \theta_D$ J_5 is constant and so

$$\rho_P \sim T^5 \quad . \tag{2.6}$$

This behavior is verified experimentally for many metals.

For non-cubic materials, the resistivity and conductivity are second rank tensors. Now the Fermi surface of a hexagonal lattice has hexagonal symmetry and thus from Equation 2.1 it follows that the principal axes are the a-axis ($<11\bar{2}0>$ direction), the b-axis ($<10\bar{1}0>$ direction), and the c-axis ($<0001>$ direction). Furthermore, Boas and Mackenzie (25) have shown that there will be no anisotropy in the basal plane of a hexagonal lattice for any physical property which is represented by a linear function between two vectors. The conductivity is a function which relates the applied electric field and the current density. Hence, the electrical resistivity tensor is completely determined by measuring the resistivity when current is applied parallel to the c-axis and when current is applied parallel to either the a- or b-axis.

In the rare earths the magnetic moment arises from the incomplete 4f electron shell. The exchange interaction between a conduction electron and the 4f shells is given by the Hamiltonian

$$\mathcal{H} = N^{-1} \sum_{n=1}^{N} V_d \, \delta(\vec{r}-\vec{R}_n)(g-1) \, \vec{J}_n \cdot \vec{\sigma} \quad , \tag{2.7}$$

where N is the number of ions, V_d is the exchange integral (a measure of the overlap of the conduction electron wave function and the 4f shell wave function), $\vec{r}$ is the position vector of the conduction electron, $\vec{R}_n$ is the position of the n^{th} ion, g is the Landé g-factor, $\vec{J}_n$ is the total angular momentum of the n^{th} ion, and $\vec{\sigma}$ is the spin angular momentum of the conduction electron.

The ordered spin structures of the heavy rare earths can be expressed analytically by

$$< J_n^x > = M'J \cos (\vec{q}\cdot\vec{R}_n) \quad , \tag{2.8a}$$

$$< J_n^y > = M'J \sin (\vec{q}\cdot\vec{R}_n) \quad , \tag{2.8b}$$

$$< J_n^z > = MJ \cos (\vec{q}\cdot\vec{R}_n - \phi) \quad , \tag{2.8c}$$

where M and M' are temperature dependent amplitude functions, $\vec{q}$ is the wave vector describing the magnetic periodicity, and ϕ is a phase angle. Since, in the rare earths, the magnetic periodicity is imcommensurate with the lattice periodicity, extra planes of energy discontinuity (magnetic superzone planes) are formed. Equations 2.7 and 2.8 with first order perturbation theory predict the position, $\vec{\ell}$, of the magnetic superzone planes to be

$$\vec{\ell} = 1/2\ (\vec{\tau}\pm\vec{q}) \quad , \tag{2.9}$$

where $\vec{\tau}$ is a reciprocal lattice vector. The first order perturbation in energy is

$$E(\vec{k}) = 1/2\{E(\vec{k}) + E(\vec{k}+2\vec{\ell}) \pm [(E(\vec{k}) - E(\vec{k}+2\vec{\ell}))^2 + V_d^2 J^2 M_{\pm}^2]^{1/2}\} \quad , \tag{2.10}$$

where $E(\vec{k})$ is the unperturbed energy, $\vec{k}$ is the wave vector of an electron, and

$$M_{\pm}^2 = M^2 + 2M'^2 \pm 2M' (M^2+M'^2)^{1/2} \quad . \tag{2.11}$$

The energy gap at the new zone is given by

$$\Delta = V_d J M_{\pm} \quad . \tag{2.12}$$

The effect of magnetic superzones on an ellipsoidal Fermi surface can be

seen in Figure 2.

If the various electronic scattering mechanisms are independent, then the relaxation time can be written

$$1/\tau = 1/\tau_R + 1/\tau_P + 1/\tau_M \quad , \tag{2.13}$$

where τ_R is the defect scattering relaxation time, τ_P is the phonon scattering relaxation time, and τ_M is the spin scattering relaxation time. If the temperature is not too low, the following approximations can be made

$$\tau_R \sim \text{constant} \quad , \tag{2.14a}$$

$$\tau_P \sim T^{-1} \quad , \tag{2.14b}$$

$$\tau_M \sim V^2 \left[1 - \frac{<\vec{J}>^2}{J^2}\right] \tag{2.14c}$$

Elliott and Wedgewood (26) used Equation 2.1 and Equations 2.7 through 2.14 to calculate the temperature dependence of the resistivity for some of the heavy rare earths. They obtained the following expressions for the a-axis resistivity, ρ_a, and the c-axis resistivity, ρ_c,

$$\rho_a = \alpha_1 + \beta_1 T + \gamma_1 \left(1 - 1/2\, M^2 - M'^2\right) \quad , \tag{2.15a}$$

$$\rho_c = \frac{\alpha_2 + \beta_2 T + \gamma_2 \left(1 - 1/2\, M^2 - M'^2\right)}{1 - \Gamma(M^2 + M'^2)^{1/2}} \quad , \tag{2.15b}$$

where

$$\Gamma = (3\pi V_d J/4E_F k_F) \sum_i |\vec{\ell}_i| \quad .$$

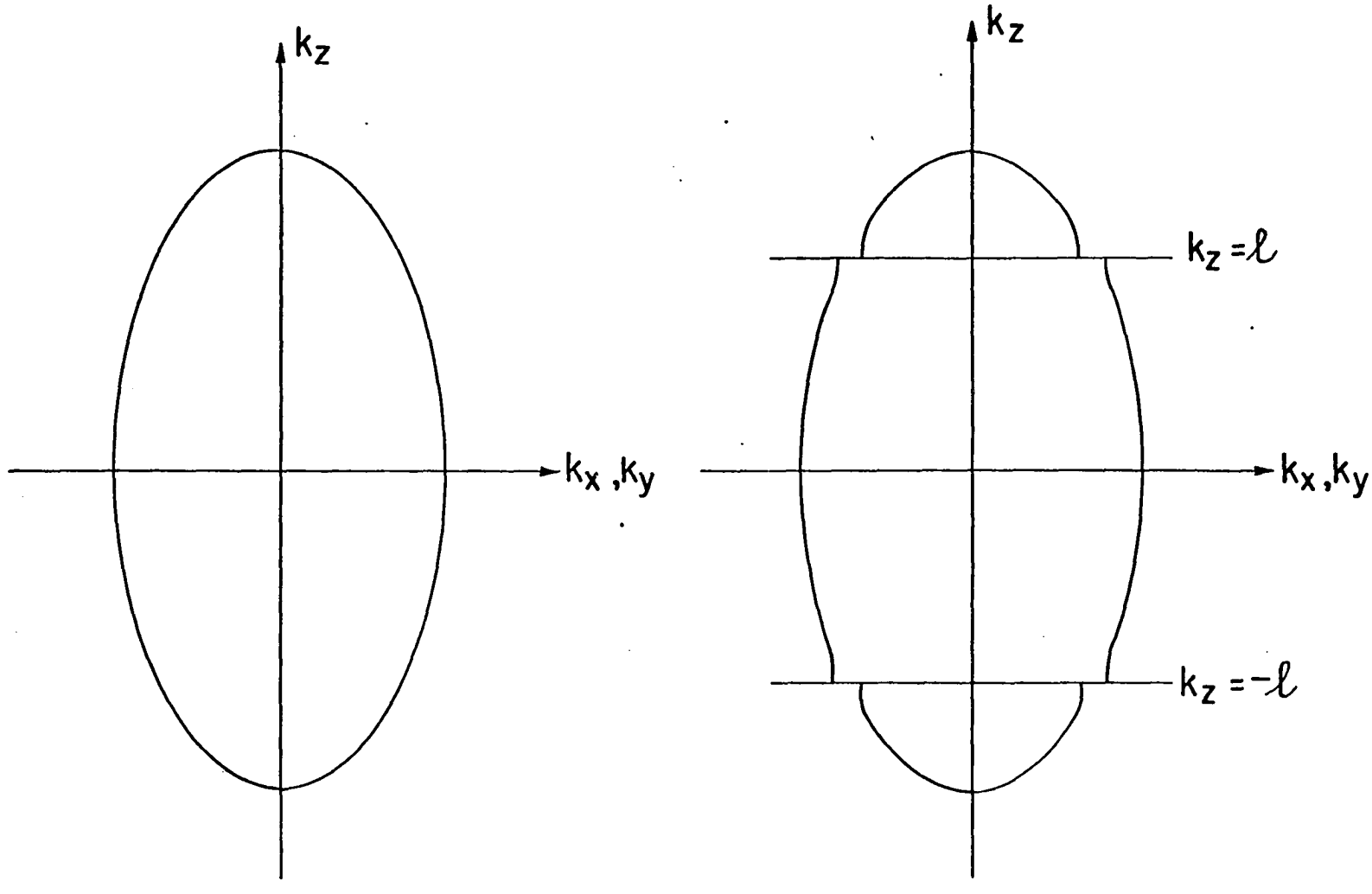

Figure 2. The effect of magnetic superzone planes ($k_z = \pm \ell$) on an ellipsoidal Fermi surface

In the last expression the sum is over all superzones which slice the Fermi surface, E_F is the Fermi energy, and k_F is the electron wave vector evaluated at the Fermi surface. α, β, γ are taken as adjustable parameters to fit the experimental data. α is a measure of the residual resistivity, β is the high temperature slope, γ is a measure of the spin disorder resistivity, and the temperature dependence of M and M' is determined by neutron diffraction measurements.

This theory predicts a maximum in ρ_c and an increase of slope in ρ_a with decreasing temperature below the ordering temperature. This agrees qualitatively with the experimental data on dysprosium, holmium, and erbium.

A serious draw-back to this theory is the assumption of an ellipsoidal Fermi surface. The Fermi surface of thulium in the paramagnetic temperature region as calculated by Freeman et al. (27) is shown in Figure 3. Shown in Figure 4 are three vertical cross-sections of the thulium Fermi surface and the effect of magnetic superzones planes. Physically, the effect of the superzone planes is to decrease the projected area of the Fermi surface along the hexagonal axis (<0001> direction). At the ordering temperature, the integral in Equation 2.1 will decrease rapidly, and thus ρ_c will increase sharply. The resistivity will also decrease below the ordering temperature because of the increase in order. This decrease coupled with the increase due to the superzone planes gives the maximum in ρ_c below the ordering temperature.

In the basal plane direction, the Fermi surface is distorted very little by the superzones and so ρ_a just decreases faster below the ordering temperature.

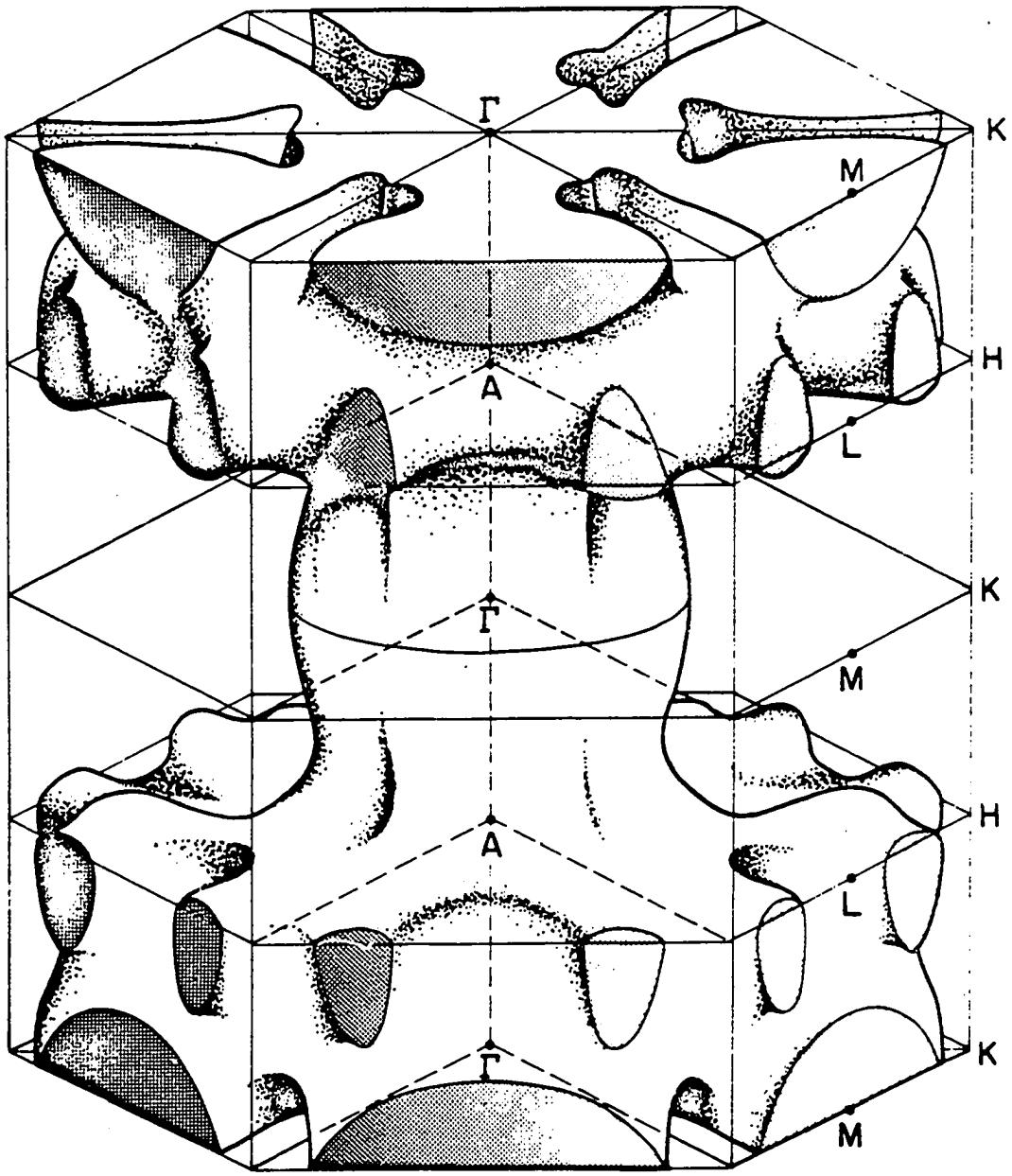

Figure 3. The complete Fermi surface for thulium as calculated by Freeman et al. (27). This is the hole surface in the double zone representation.

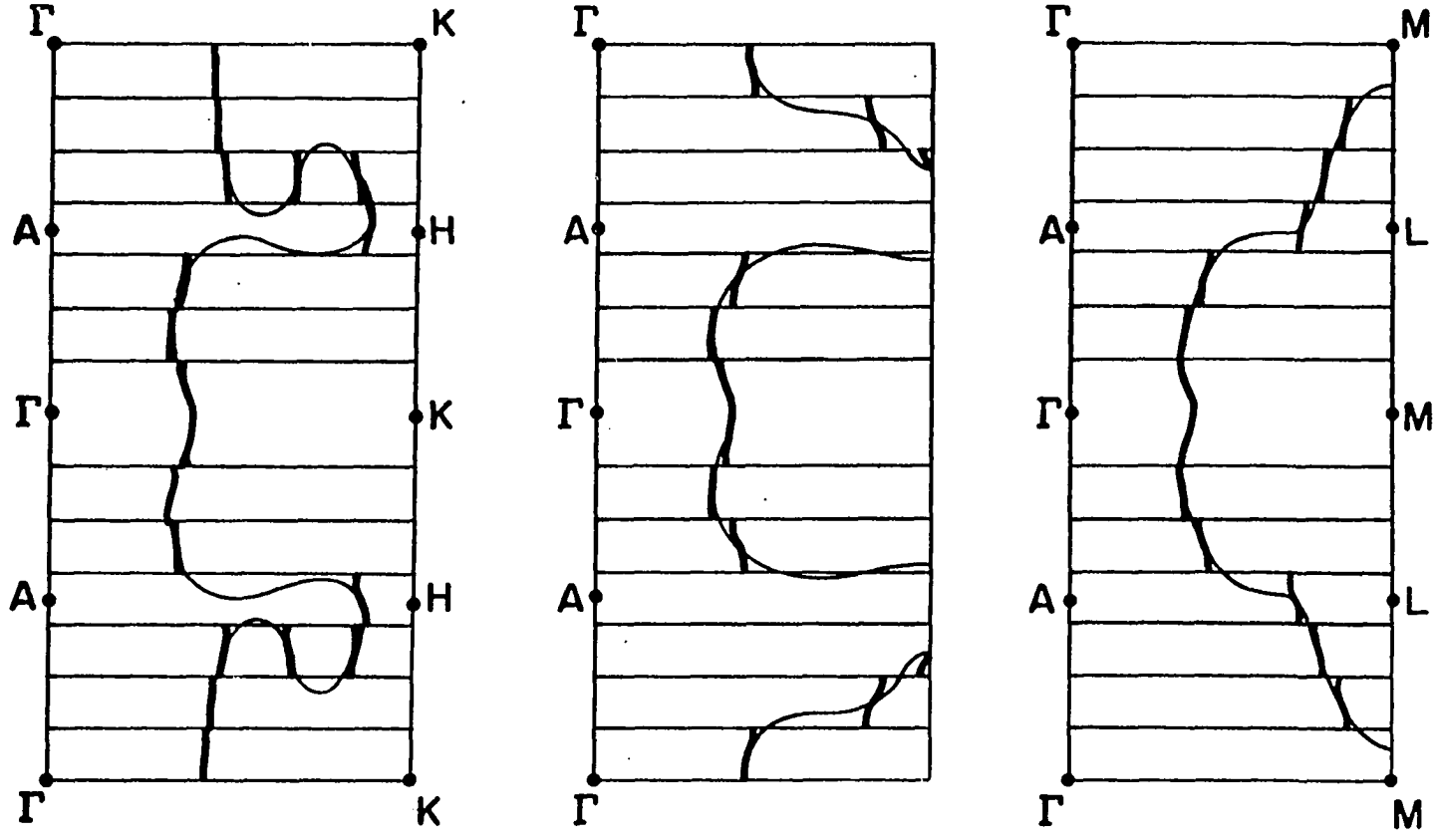

Figure 4. Some vertical cross-sections of the thulium Fermi surface. The effect of the magnetic superzones (horizontal lines) is demonstrated by comparing the paramagnetic Fermi surface (light solid line) and the perturbed Fermi surface (heavy solid lines).

Mackintosh (28) has considered the effect of spin wave scattering at low temperatures on the resistivity and has obtained the following expression

$$\rho_{sw} = CT^2 \exp(-\epsilon/kT) \quad , \tag{2.16}$$

where C is a constant, ϵ is the minimum energy to excite a spin wave, and k is the Boltzmann constant. Because of the high impurity scattering at low temperatures a comparison with experiment is difficult to make.

Above the ordering temperature the magnetic moments are disordered which results in a spin-disorder resistivity, $\rho_{s\sim}$. Dekker (29) used the exchange interaction (Equation 2.7) and a spherical Fermi surface to obtain the following expression for the spin-disorder resistivity in the rare earths

$$\rho_{s\sim} = (3\pi Nm/2\hbar e^2 E_F)\, V_d^2\, (g-1)^2\, J(J+1) \quad , \tag{2.17}$$

where N is the number of atoms, m is the electronic mass, and the rest of the symbols are as defined earlier. This expression predicts $\rho_{s\sim}$ is independent of temperature in agreement with experiment. This expression, however, does not predict the anisotropy in $\rho_{s\sim}$ which is observed experimentally in the single crystal data.

B. Seebeck Coefficients

In the presence of an electric field, $\vec{E}$, and a temperature gradient, ∇T, the current flux, $\vec{J}$, and the energy flux, $\vec{U}$, in a metal are expressed by

$$\vec{J} = L_{EE} \cdot \vec{E} + L_{ET} \cdot \nabla T \quad , \tag{2.18a}$$

$$\vec{U} = L_{TE}\cdot\vec{E} + L_{TT}\cdot\nabla T \quad , \tag{2.18b}$$

where the coefficients are tensors. The justification of these equations follows from the linearity of the Boltzmann integral equation (23,p.270).

If $\nabla T = 0$ and $\vec{E} \neq 0$, then $\vec{J} = L_{EE}\cdot\vec{E}$ and $\vec{U} = L_{TE}L_{EE}^{-1}\cdot\vec{J}$. Thus the electrical conductivity, σ, and the Peltier coefficient, Π, are related to the transport coefficients by

$$\sigma = L_{EE} \quad , \tag{2.19}$$

$$\Pi = L_{TE}L_{EE}^{-1} \quad . \tag{2.20}$$

If $\vec{J} = 0$, then $\vec{E} = L_{EE}^{-1}L_{ET}\cdot\nabla T$ and $\vec{U} = (L_{TT}-L_{TE}L_{EE}L_{TE})\cdot\nabla T$. The Seebeck coefficient, S, and the thermal conductivity, K, are given by

$$S = -L_{EE}^{-1}L_{ET} \quad , \tag{2.21}$$

$$K = (L_{TT}-L_{TE}L_{EE}^{-1}L_{TE}) \quad . \tag{2.22}$$

The coefficients in Equation 2.18 are not completely independent; for it can be shown by the application of Onsager's theorem (23,p.273) to Equation 2.18 that

$$TL_{ET} = -L_{TE} \quad . \tag{2.23}$$

Thus it is sufficient to measure the electrical conductivity, thermal conductivity, and the Seebeck coefficient to completely determine the coefficients in Equations 2.18. The first Kelvin relation is

$$\Pi = ST \quad , \tag{2.24}$$

which is obtained by substituting Equations 2.20 and 2.21 into Equation 2.23.

If both a heat current and an electrical current are flowing in a metal, then the increase of energy per unit volume, $\dot{Q}$, is

$$\dot{Q} = \vec{E}\cdot\vec{J} - \nabla\cdot\vec{U} \quad . \tag{2.25}$$

Equation 2.25 can be written in terms of σ, K, and S and is given by

$$\dot{Q} = (\sigma^{-1}\cdot\vec{J})\cdot\vec{J} + \nabla\cdot(K\cdot\nabla T) - (T\frac{\partial S}{\partial T})\cdot(\vec{J}\cdot\nabla T) \quad , \tag{2.26}$$

where the first term is the irreversible Joule heat produced by the current $\vec{J}$, the second term is the net flow of heat, and the last term is the reversible Thomson heat. The coefficient of $\vec{J}\cdot\nabla T$ is the Thompson coefficient, μ, and is given by

$$\mu = T(\partial S/\partial T) \quad , \tag{2.27}$$

(the second Kelvin relation).

In the relaxation time approximation formal transport theory gives the following expression for the Seebeck coefficients (23,p.379)

$$S_{ij} = (\pi^2 k^2 T/3e) \sum_l [\sigma_{il}^{-1}(E) \frac{d}{dE} \sigma_{lj}(E)]_{E = E_F} \quad , \tag{2.28}$$

where

$$\sigma_{ij}(E) = (e^2/4\pi^3\hbar) \int_{\vec{E}} \tau\, v_i\, dA_j \quad . \tag{2.29}$$

For cubic symmetry Equations 2.29 and 2.28 become

$$\sigma(E) = (e^2/12\pi^3\hbar) \int_E \tau v d\mathcal{S} \quad , \tag{2.30}$$

$$S = (\pi^2 k^2 T/3e) \left[\frac{d}{dE} \ln\sigma(E)\right]_{E = E_F} \quad . \tag{2.31}$$

If the mean free path, $\Lambda(E) = \tau(E)v(E)$, is a slowly varying function at the Fermi surface, then Equations 2.30 and 2.31 become

$$\sigma(E) = (e^2/12\pi^3\hbar)\, \Lambda(E)\, \Sigma(E) \quad , \tag{2.32}$$

$$S = (\pi^2 k^2 T/3e) \left[\frac{d}{dE} \ln \Lambda(E) + \frac{d}{dE} \ln \Sigma(E)\right]_{E = E_F} \quad , \tag{2.33}$$

where

$$\Sigma(E) = \int_E d\mathcal{S} \quad . \tag{2.34}$$

In Equation 2.33 the sign of the second term depends upon the detailed geometry of the zone: it is positive for electron surfaces and is negative for hole surfaces. If the energy dependence of Λ can be neglected, then $S < 0$ for electron surfaces and $S > 0$ for hole surfaces.

For magnetic materials there are <u>three</u> sources of thermoelectricity: electron diffusion, phonon drag, and magnon drag. To a first approximation these sources of thermoelectricity are independent (30,p.113) so that the total Seebeck coefficient is just the sum

$$S = S_D + S_P + S_M \quad , \tag{2.35}$$

where S_D is the electron diffusion coefficient, S_P is the phonon drag coefficient, and S_M is the magnon drag coefficient.

If the Fermi surface is spherical and the mean free path is independent of energy, then by Equation 2.33 the electron diffusion coefficient is

$$S_D = (\pi^2 k^2 T/3eE_F) \quad . \tag{2.36}$$

Thus the electron diffusion coefficient is a linear function of temperature.

Since $\nabla T \neq 0$, the phonons are not in thermodynamic equilibrium, but are moving as a heat current. At high temperatures (temperatures greater than the Debye temperature, θ_D) the phonon mean free path is short and the asymmetry of the phonon distribution is not communicated to the electrons. However, at low temperatures ($T < \theta_D$) the phonon mean free path is long and the electrons are dragged along by the phonon current. Ziman (23,p.409) and MacDonald (30,p.101) have shown for normal processes that

$$S_P \sim T^3/e, \; T < \theta_D \quad ; \tag{2.37a}$$

$$S_P \sim 1/eT, \; T \gtrsim \theta_D \quad : \tag{2.37b}$$

$$S_P \sim \text{constant}/e, \; T > \theta_D \quad . \tag{2.37c}$$

These equations predict a phonon drag peak around $\theta_D/10$ to $\theta_D/5$, which is in fair agreement with experiment. If Umklapp processes predominate, then $S_P > 0$ and if $|S_P| > |S_D|$ then the total Seebeck coefficient can change sign.

Besides the phonon energy current, in the rare earths there will also be a magnon current. Bailyn (31) finds for normal processes identical temperature dependences for S_M and S_P. Furthermore, he shows S_M can change sign for Umklapp processes. Because phonon and magnon drag effects overlap, it is difficult in practice to distinguish between them. Generally the

magnon drag peaks will be found around 20°K, however, recently Blatt et al. (32) have found magnon drag peaks in iron at 200°K.

Since the Seebeck coefficient is the most sensitive of the transport coefficients to the electronic structure magnetic superzone planes will have a dramatic effect. Mackintosh [c.f. Sill (33,p.107)] has extended the theory of Elliott and Wedgewood (26) and has obtained the following expressions for the a-axis Seebeck coefficient, S_a, and the c-axis Seebeck coefficient, S_c,

$$S_a = (\pi^2 k^2 T/2eE_F)[3-\rho_M/\rho] \quad , \tag{2.38a}$$

$$S_c = (\pi^2 k^2 T/2eE_F)[3/(1-\delta)-\rho_M/\rho] \quad , \tag{2.38b}$$

where ρ_M is the magnetic scattering resistivity, ρ is the total resistivity, and

$$\delta = (3\pi/4)\ (|\vec{\tau}|/k_F)\ (\Delta/E_F) \quad .$$

The symbols in the last equation are defined in Equation 2.15. Equations 2.38 predict that S_a will increase and S_c will decrease below the ordering temperature. For the heavy rare earths, the agreement with experiment is poor.

The rare earths have three electrons in the 5d and 6s conduction bands. The total Seebeck coefficient is not the algebraic sum of the Seebeck coefficients for each carrier, but the weighted sum

$$S = \sum_i \sigma_i S_i / \sum_i \sigma_i \quad , \tag{2.39}$$

where σ_i is the electrical conductivity of carrier i and S_i is the Seebeck

coefficient of carrier i.

If there is one group of carriers, but several independent scattering mechanisms, then the total Seebeck coefficient is given by another weighted sum

$$S = \sum_i (S_i/K_i) \; / \; \sum_i (1/K_i) \quad , \tag{2.40}$$

where K_i is the thermal conductivity due to the i^{th} scattering mechanism and S_i is the Seebeck coefficient characteristic of the i^{th} scattering mechanism. The derivation of Equations 2.39 and 2.40 are given by MacDonald (30).

C. Thermal Conductivity

In non-magnetic metals heat is transported by electrons and phonons. To a first approximation these carriers are assumed to be independent, and the total thermal conductivity, K, is given by the algebraic sum

$$K = K_L + K_E \quad , \tag{2.41}$$

where K_L is the lattice thermal conductivity (due to phonon carriers) and K_E is the electronic thermal conductivity (due to the conduction electrons). For magnetic materials magnons can also transport heat and in the above approximation the total thermal conductivity is

$$K = K_L + K_E + K_M \quad , \tag{2.42}$$

where K_M is the thermal conductivity associated with the magnon carriers.

Thermal resistance arises from the scattering of the carriers by their environment. Phonons are scattered by the conduction electrons, boundaries, other phonons, and magnetic moments. If the various scattering mechanisms

are independent (Matthiessen's rule) the lattice thermal resistance, $W_L = 1/K_L$, can be written

$$W_L = W_P^P + W_P^E + W_P^B + W_P^I + W_P^M \quad , \qquad (2.43)$$

where W_P^P, W_P^E, W_P^B, W_P^I, and W_P^M are the lattice thermal resistances due to phonon-phonon, phonon-electron, phonon-boundary, phonon-impurity, and phonon-magnetic moment scattering respectively.

From kinetic theory the thermal conductivity of a group of carriers is given by

$$K = 1/3\ C\bar{v}\ \Lambda \quad , \qquad (2.44)$$

where C, $\bar{v}$, and Λ are the specific heat, average speed, and mean free path of the carrier respectively. At high temperatures, $T > \theta_D$, the mean square displacement of an atom is proportional to the absolute temperature. Thus $\Lambda \sim 1/T$, and since $C \sim$ constant in this temperature range, the thermal conductivity becomes

$$K_P^P = 1/W_P^P \sim s/T \quad , \qquad (2.45)$$

where s is the speed of sound in the crystal.

Phonon-phonon scattering processes are described by the momentum and energy relationships

$$\vec{q} + \vec{q}' = \vec{q}'' + \vec{\tau} \qquad (2.46a)$$

$$\hbar\nu + \hbar\nu' = \hbar\nu'' \quad , \qquad (2.46b)$$

where $\vec{q}$ and $\vec{q}'$ are the wave vectors of the interacting phonons, $\vec{q}''$ is the wave vector of the resultant phonon, $\vec{\tau}$ is a reciprocal lattice vector, ν

ν' are frequencies of the interacting phonons, and ν'' is the frequency of the resultant phonon. Peierls (34) has pointed out that for N-processes ($\vec{\tau} = 0$) the phonon energy is redistributed into different phonons without altering the total energy flow. Hence, the thermal resistivity for N-processes is zero. In U-processes ($\vec{\tau} \neq 0$) if energy is to be conserved (23)

$$\hbar\nu'' \gtrsim k\theta_D/2 \quad , \tag{2.47}$$

and the rate at which these processes occur is proportional to

$$\exp(-\hbar\nu/kT) \exp(-\hbar\nu'/kT) \lesssim \exp(-\theta_D/2T) \quad . \tag{2.48}$$

Hence, $\Lambda \sim \exp(\theta_D/2T)$ and in the limit $T < \theta_D$, $C \sim (T/\theta_D)^3$. Thus from Equation 2.44

$$K_P^P = 1/W_P^P \sim s(T/\theta_D)^3 \exp(\theta_D/2T) \quad . \tag{2.49}$$

Equations 2.45 and 2.49 are derived rigorously by solving the linearized Boltzmann equation (23).

For $T \ll \theta_D$, Λ is of the order of centimeters and is limited by the physical size of the sample. The thermal resistance for boundary scattering is given by

$$K_P^B = 1/W_P^B \sim s/T^3 \quad . \tag{2.50}$$

The temperature dependence of the thermal conductivity for phonon-phonon and phonon-boundary scattering is summarized by the dotted curve in Figure 5.

The phonon-electron scattering process is expressed by

$$\vec{q} + \vec{k} = \vec{K}' \quad , \tag{2.51}$$

where $\vec{k}$ and $\vec{k}'$ are the initial and final electron wave vectors respectively. Ziman (23,p.319) shows that if the phonons interact with a gas of free electrons in equilibrium, the thermal resistivity can be expressed by

$$W_P^E \leq (\rho_L/T)\ (n_a e/k)^2\ (3Nk/C)^2 \quad , \tag{2.52}$$

where ρ_L is the lattice electrical resistivity, N is the number of atoms, and n_a is the number of conduction electrons per atom. The equality holds for N-processes, while the inequality is for U-processes. In the limit $T > \theta_D$, $C \sim eNk$, and $\rho_L \sim T$. Thus

$$K_P^E = 1/W_P^E \sim (k/en_a)^2 \quad . \tag{2.53}$$

In the opposite limit $T < \theta_D$, $C \sim T^3$, and $\rho_L \sim T^5$. Therefore,

$$K_P^E = 1/W_P^E \sim T^2 \quad . \tag{2.54}$$

The thermal conductivity for phonon-electron scattering is shown by the dashed curve in Figure 5.

The temperature dependence of the phonon-impurity lattice resistivity varies with the type of impurity. The general effects of impurity scattering, however, is to lower the maximum of the lattice thermal conductivity.

In magnetic materials, the magnetic moments will also scatter phonons. Very little theoretical work has been done on this problem, although Stern (35) has shown that the phonon-magnetic moment interaction leads to a sharp dip in the thermal conductivity at the transition temperature. This

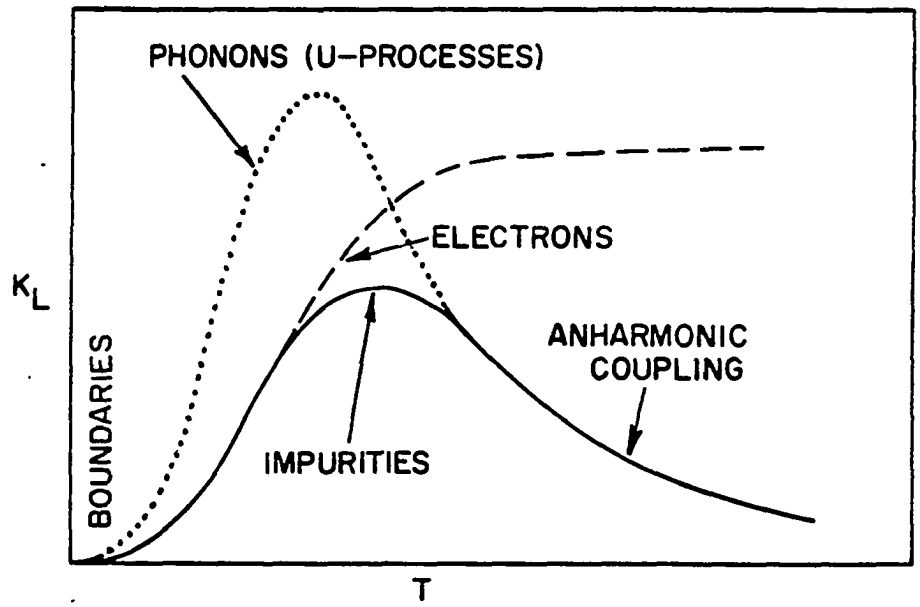

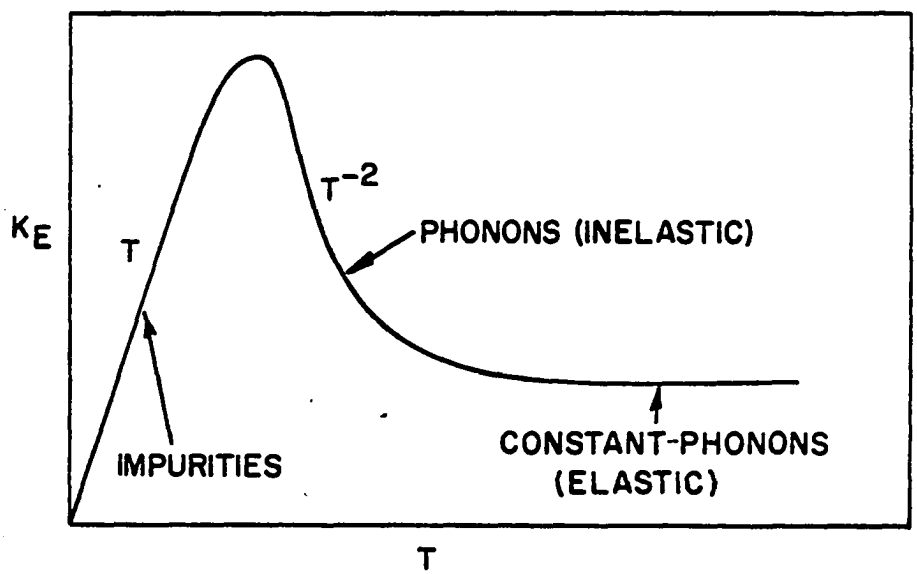

Figure 5. The lattice and electronic thermal conductivity of a metal

is in qualitative agreement with the observed thermal conductivity of CoF_2.

In most metals the electrons transport the major portion of the thermal energy. The conduction electrons are scattered by phonons, other conduction electrons, impurities, and magnetic moments. If the various scattering mechanisms are independent, the electronic thermal resistance, $W_E = 1/K_E$, can be written as the sum

$$W_E = W_E^P + W_E^E + W_E^I + W_E^M \quad , \tag{2.55}$$

where the superscripts indicate the scattering mechanisms.

If the electronic scattering is elastic and can be described by a relaxation time, τ, then from formal transport theory (23) the electronic thermal conductivity for the principal axes is given by

$$(K_E)_{ii} = L_0 T \left[\sigma_{ii}(E_F) - L_0 \sigma_{ii}^{-1} (E_F) \left(\partial\sigma_{ii}/\partial E\right)_{E_F}\right] \quad , \tag{2.56}$$

where

$$L_0 = k^2\pi^2/3e^2 \quad , \tag{2.57}$$

is the Lorenz number, and

$$\sigma_{ii}(E) = (e^2/4\pi^3\hbar \int_E \tau \, v_i \, d\ell_i \quad , \tag{2.58}$$

is the electrical conductivity. The second term in Equation 2.56 is generally small and can be neglected. Thus

$$(K_E)_{ii} = L_0 T \sigma_{ii} (E_F) \quad ,$$

or in terms of the electrical resistivity tensor

$$(K_E)_{ii}\,\rho_{ii}/T = L_0 \quad . \tag{2.59}$$

This is the Wiedemann-Franz law and it is exactly obeyed if the electronic scattering is elastic. A general Lorenz function, L, can be defined as

$$L = K\rho/T \quad , \tag{2.60}$$

where K and ρ are experimentally determined. L is plotted as a function of temperature and regions in which L is independent of T the electronic scattering is elastic, while in regions where L is dependent on T the electronic scattering is inelastic. In what follows the principal axes notation will be dropped for clarity.

In electron-phonon interactions the quantized energy of a phonon can be gained or lost by the electron, and so the process can be very inelastic. Ziman (23,p.385) using the variational technique to solve the Boltzmann equation for electron-phonon scattering derives the following expression for electronic thermal resistivity

$$W_E^P = (4\rho_\theta/L_0T)\,[(T/\theta_D)^5\,\{J_5(\theta_D/T) - (1/2\pi^2)\,J_7(\theta_D/T)\}$$

$$+ (3/\pi^2)\,(\mathcal{R}/\mathcal{D})^2\,(T/\theta_D)^3\,J_5(\theta_D/T)] \quad , \tag{2.61}$$

where J_5 and J_7 belong to the class of Debye integrals, ρ_θ is a constant, $\mathcal{R}$ is the Fermi radius, and $\mathcal{D}$ is the Debye radius. In the limit $T < \theta_D$ Equation 2.61 becomes

$$W_E^P = 1/K_E^P \sim T^2 \quad , \tag{2.62}$$

while in the opposite limit $T > \theta_D$

$$W_E^P = 1/K_E^P \rightarrow \rho_L/L_0T \sim \text{constant} \quad . \tag{2.63}$$

At high temperatures the Wiedemann-Franz law is obeyed and the electron-phonon scattering is elastic.

Electron-impurity scattering is generally elastic and the thermal resistance can be calculated from the Wiedemann-Franz law. The residual electrical resistivity is independent of temperature and so

$$W_E^I = 1/K_E^I \sim T \quad . \tag{2.64}$$

If only impurities and phonons are the important scattering mechanisms, the electronic thermal resistivity becomes

$$W_E = A/T + BT^2 \quad . \tag{2.65}$$

This equation predicts a maximum in the thermal conductivity for $T < \theta_D$. The electronic thermal conductivity of a typical metal is shown in Figure 5. Equation 2.65 can be rewritten as

$$T/K_E = A + BT^3 \quad . \tag{2.66}$$

The linearity of a T/K versus T^3 plot, where K is the experimentally measured thermal conductivity, will indicate if the electron-phonon and electron-impurity are the dominant scattering mechanisms for $T < \theta_D$.

Just as in the case of phonon-phonon scattering only U-processes give a finite resistivity for electron-electron scattering. Ziman (23) predicts that $W_E^E \sim T^2$ and should be large enough to observe in a monovalent metal such as sodium. However, experimentally this effect has not been observed.

The conduction electrons are scattered elastically by paramagnetic moments. This is verified experimentally in that the spin-disorder resistivity, ρ_s is independent of temperature (cf. Equation 2.17). Thus from the Wiedemann-Franz law

$$W_E^{PM} \sim 1/T \quad . \tag{2.67}$$

Kasuya (36), using the s-d interaction model, calculated the transport coefficients for ferromagnetic metals and alloys. He does not obtain an explicit expression for the temperature dependence of the thermal conductivity, but does indicate that the Lorenz function is temperature dependent. His method could be carried over to the rare earths by the use of an s-f exchange interaction model.

The effect of magnetic superzones is to redistribute the states into which the conduction electrons can scatter. This will have a profound effect on the electronic thermal resistivity. The effect of superzones will be discussed in more detail in section V.

In magnetic metals how much heat the magnons transport is still an unanswered question. Magnons are scattered by the same particles and quasi-particles as phonons. If the scattering mechanisms are independent the magnon thermal resistivity is given by

$$W_M = W_M^M + W_M^P + W_M^E + W_M^I + W_M^B \quad . \tag{2.68}$$

Kasuya (36) shows that for temperatures below $10^{\circ}K$ the magnon free path is determined by the sample dimensions. The magnon specific heat is $C_M \sim T^{3/2}$ and so from Equation 2.44

$$W_M^B \sim T^{-3/2} \quad . \tag{2.69}$$

Kasuya also shows that the thermal resistivity for magnon-magnon scattering will be zero for both U-processes and N-processes. At present there are no theoretical expressions for the other terms in Equation 2.68.

The final subject to be considered in this section is the experimental separation of K_L, K_E, and K_M (cf. Equation 2.42). At high temperatures the electronic scattering is elastic and K_E can be determined from the Wiedemann-Franz law

$$K_E = L_0 T/\rho \quad , \tag{2.70}$$

where ρ is the experimentally measured resistivity of the same specimen which was used in the thermal conductivity measurements. If magnon carriers are unimportant at high temperatures, then the lattice thermal conductivity can be found from Equation 2.41

$$K_L = K - L_0 T/\rho \quad . \tag{2.71}$$

If at high temperatures only electron-phonon interactions are important, then from Equations 2.52 and 2.62

$$K_L = (k/en_a)^2 \, (T/\rho_L) \quad ,$$

$$K_E = 1/3 \, (\pi k/e)^2 \, (T/\rho_L) \quad ,$$

and

$$K_L \sim (3/n_a^2 \, \pi^2) K_e \quad .$$

Thus for a monovalent metal $K_L \sim K_E$. In practice, however, $W_P^P \gg W_P^E$ and

$K_E \gg K_L$. If impurities are a dominant mechanism in the scattering of electrons, then the lattice thermal conductivity can be of the same order of magnitude as the electronic thermal conductivity. At present there is no way of disentangling K_M from K_L.

III. EXPERIMENTAL PROCEDURE

A. Sample Preparation

The thulium used in this study was separated from the other rare earths by the ion exchange process (37) at the Ames Laboratory.

Single crystals of all the heavy rare earths except thulium and ytterbium have been grown by the strain anneal technique (38). The strains which nucleate the grain growth in the annealing process are induced thermally by arc-melting on a cold copper hearth. Temperatures near the melting temperature in the annealing process are necessary for the grain boundaries to have sufficient energy to move.

In the early attempts to grow thulium single crystals, the metal would sublime in the annealing process because of its high vapor pressure. This problem was solved by suspending the arc-melted button in a 1 in. diameter tantalum crucible. The tantalum crucible was sealed under 0.5 atm. of helium in an arc-welder. The small volume of the crucible allowed the thulium button and its vapor to come into equilibrium with a loss of less than 5% of the button.

The annealing furnace is shown in Figure 6. This furnace has a gradient temperature region ($25^{\circ}C$/cm.) and a constant temperature region. To get optimum grain growth for thulium, the following annealing program was used: 12 hours at $1200^{\circ}C$ in the gradient region, 12 hours at $1300^{\circ}C$ in the gradient region, and 16 hours at $1425^{\circ}C$ in the constant temperature region. Single crystals on the order of 1 x 1 x 2 cm. were observed. The grain size was limited by the size of the arc-melted button. Because of the vapor pressure problem, large arc-melted buttons were impossible to get. An alternate method, to get a larger strained specimen, might be to

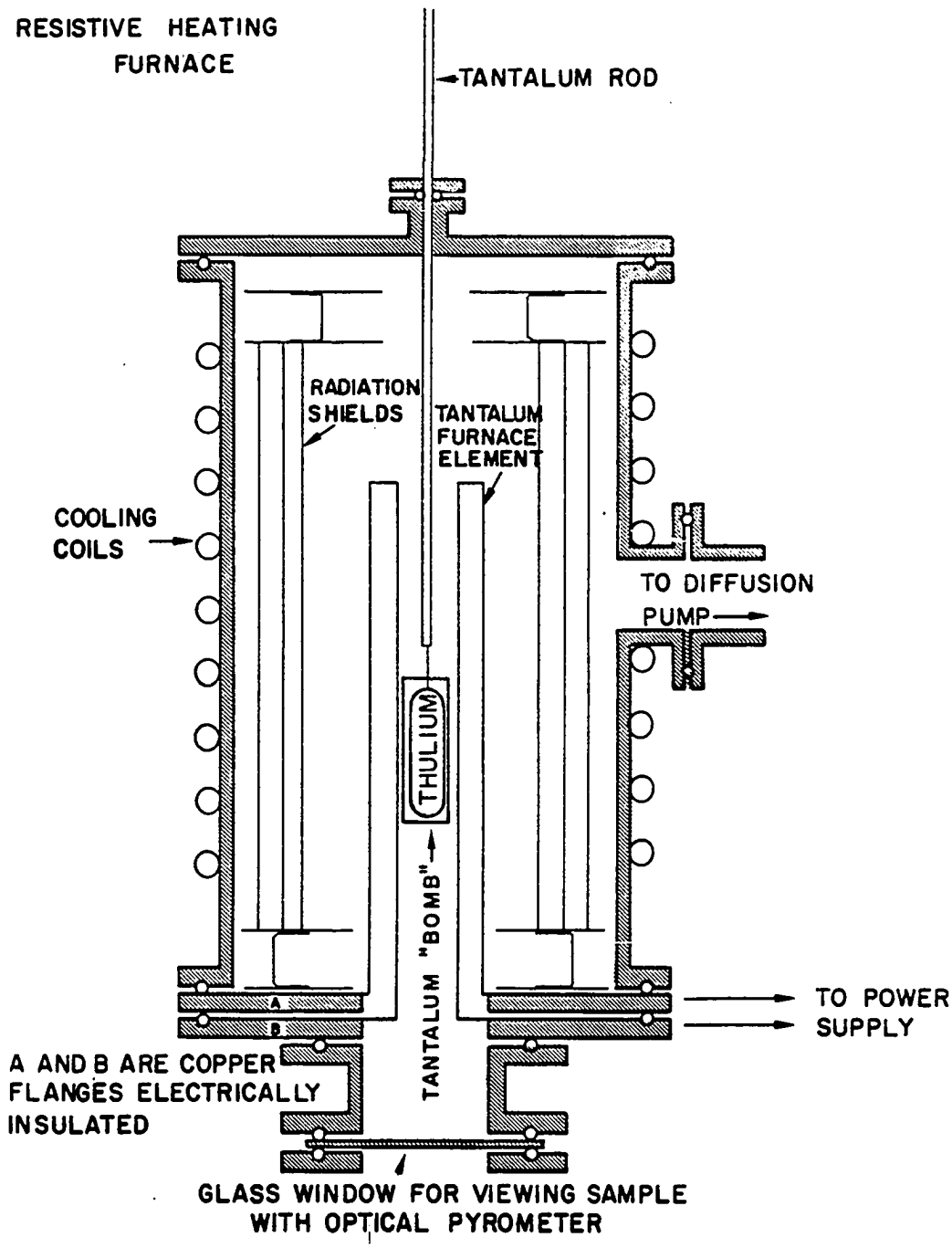

Figure 6. The annealing furnace used for growing single crystals

first cast the thulium into a cylinder inside a sealed tungsten crucible and then strain the cylinder mechanically.

The crystals were oriented by Laue back reflection of X-rays. The samples were cut to the approximate dimensions by a Servomet spark erosion apparatus and then hand lapped to the final dimensions with carborundum paper. The samples were in the form of rectangular parallelepipeds with the approximate dimensions of 1 x 1 x 6 mm. The sample dimensions were measured with a Steinmeyer 25-50 mm. metric micrometer and a 25 mm. gauge block. This instrument was accurate to within $\pm$ 0.001 mm. The a-axis, - b-axis, and c-acis crystals were cut such that the a, b, and c axes were respectively parallel to the long dimension. The sample dimensions are listed in the Appendix.

Impurity analyses were made on scrap material of the button from which the single crystals were cut. A quantitative vacuum fusion analysis was made for the dissolved gas impurities and a semi-quantitative analysis was made for the other impurities. Sample impurities and resistivity ratios are listed in the Appendix. Twins were also observed after the button had been etched. It was estimated that they occupied approximately 1% of the total volume of a crystal.

B. Measurement of the Electrical Resistivity

If a metal of cross-sectional area, A, is carrying a current, I, a voltage per unit length, V/L, will be developed parallel to the direction of the current and is given by

$$V/L = \rho\ I/A \quad , \tag{3.1}$$

where ρ is the electrical resistivity.

The electrical resistivity was measured as a function of temperature from 1.3 to 300°K by the standard 4-probe technique. The resistivity measuring circuit is shown in Figure 7 and the circuit of the constant current supply is shown in Figure 8. The voltage, V, was measured with a Honeywell model 2768 six dial potentiometer, Guildline 5214/9660 photocell galvanometer amplifier, and a Guildline type SR21/9461 secondary galvanometer. The voltage, V, could be read with a resolution of 0.01 microvolts with this system. The current, I, was measured with a 0.1 ohm standard resistor. The voltage across the standard resistor was measured with a Leeds and Northrup type K-3 potentiometer and a Leeds and Northrup type 9834 null detector. The current was measured to five significant figures. Since thermal emfs generally have a constant sign, they were eliminated by measuring the voltage, V, with forward and reverse current.

The sample holder and voltage probes are shown in Figure 9. The distance, L, between the voltage contacts was measured on a traveling microscope. This instrument was accurate to within $\pm$ 0.0001 cm. The samples were electropolished and the ends were tinned with indium solder by using an ultrasonic soldering gun. The current leads were then soldered to the ends of the sample. The voltage contacts were held in place under the tension of a spring.

The sample temperature was measured by thermocouples anchored directly beneath the sample. For temperatures above 25°K a Cu versus constantan thermocouple was used, while a Cu versus AuFe thermocouple was used below 25°K. Because of the low melting temperature of the AuFe wire, indium solder was used to make the thermocouple junctions. The calibration used for the Cu versus constantan thermocouple was that of Powell *et al.* (39).

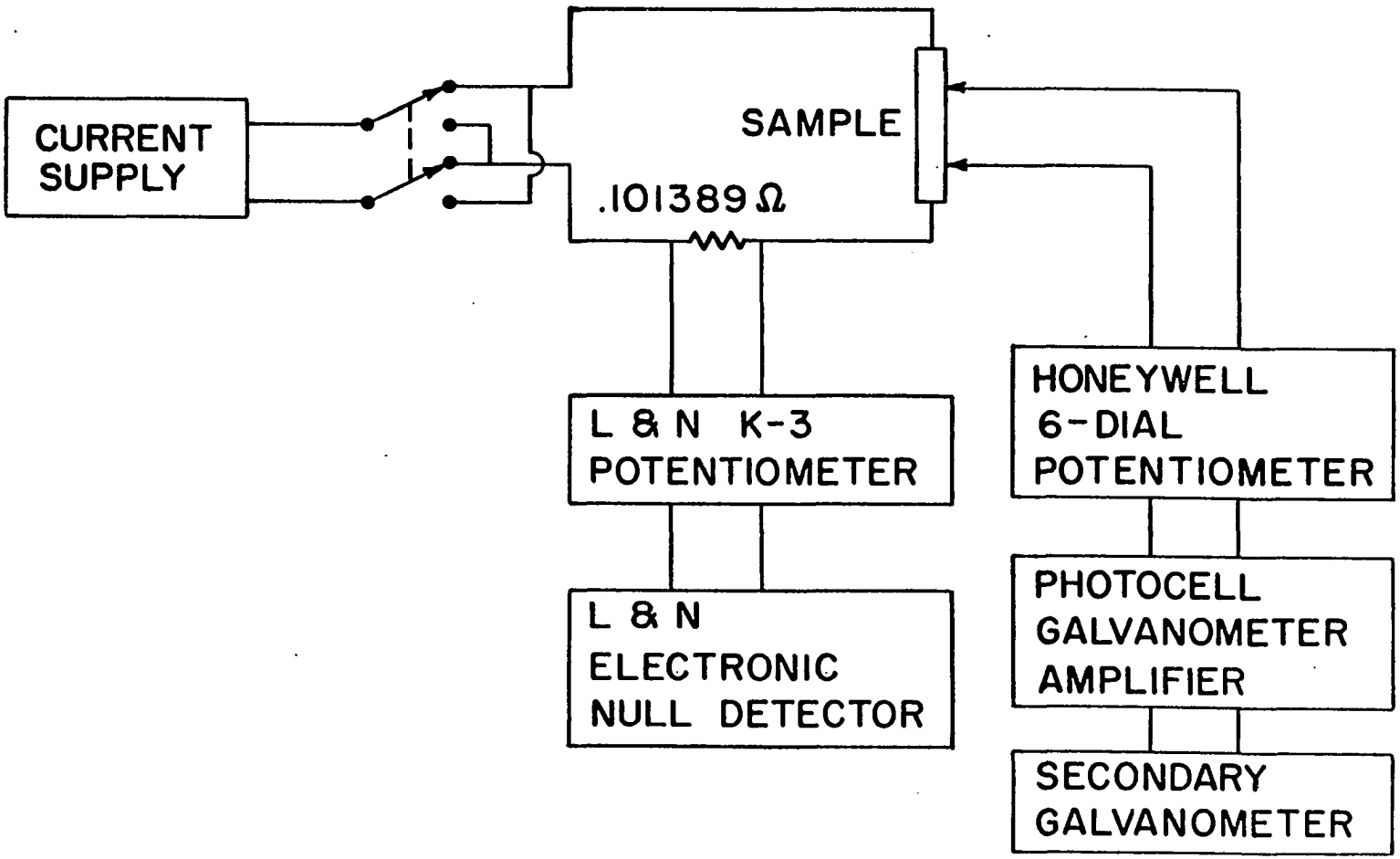

Figure 7. The circuit for measuring the electrical resistivity

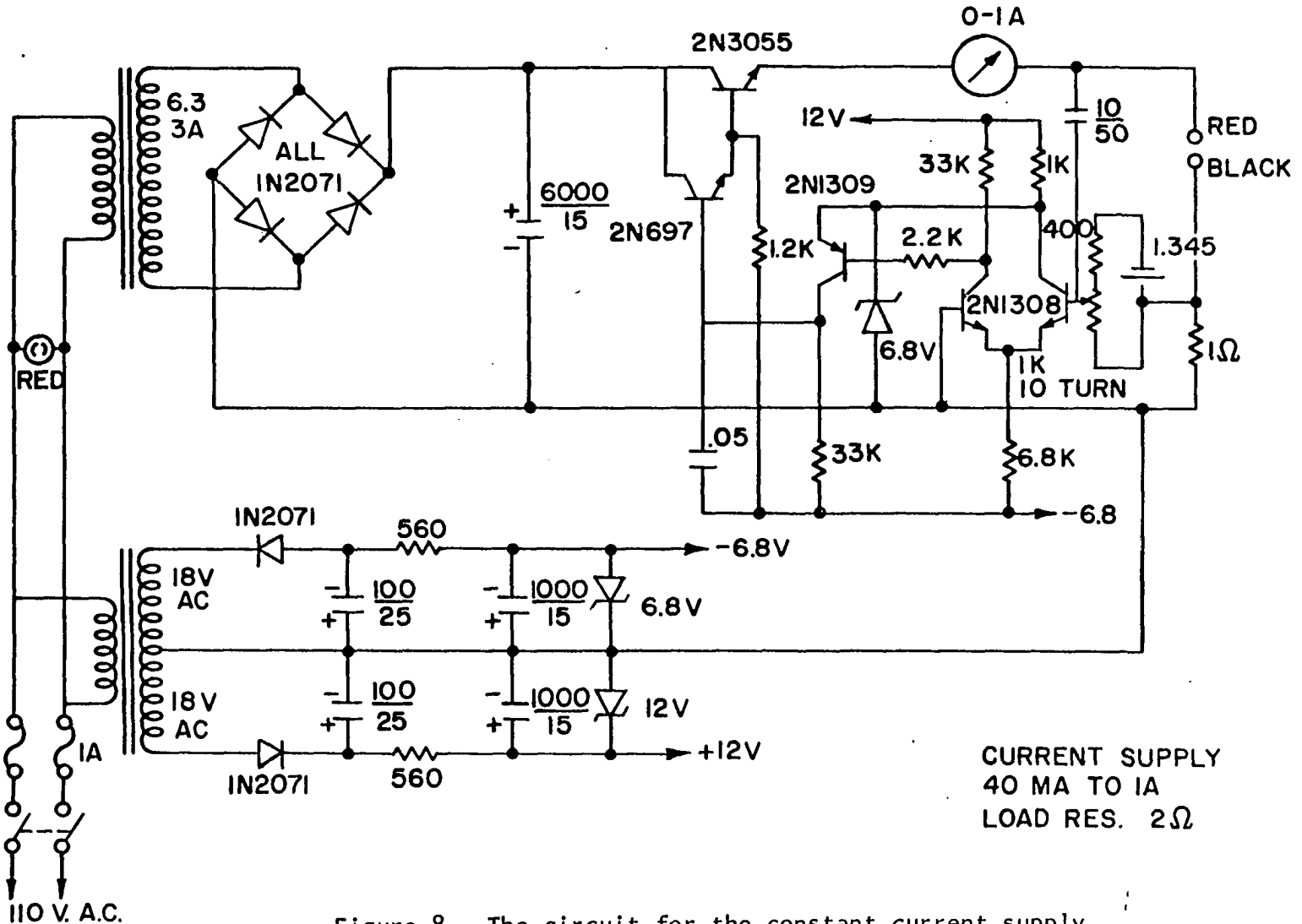

Figure 8. The circuit for the constant current supply

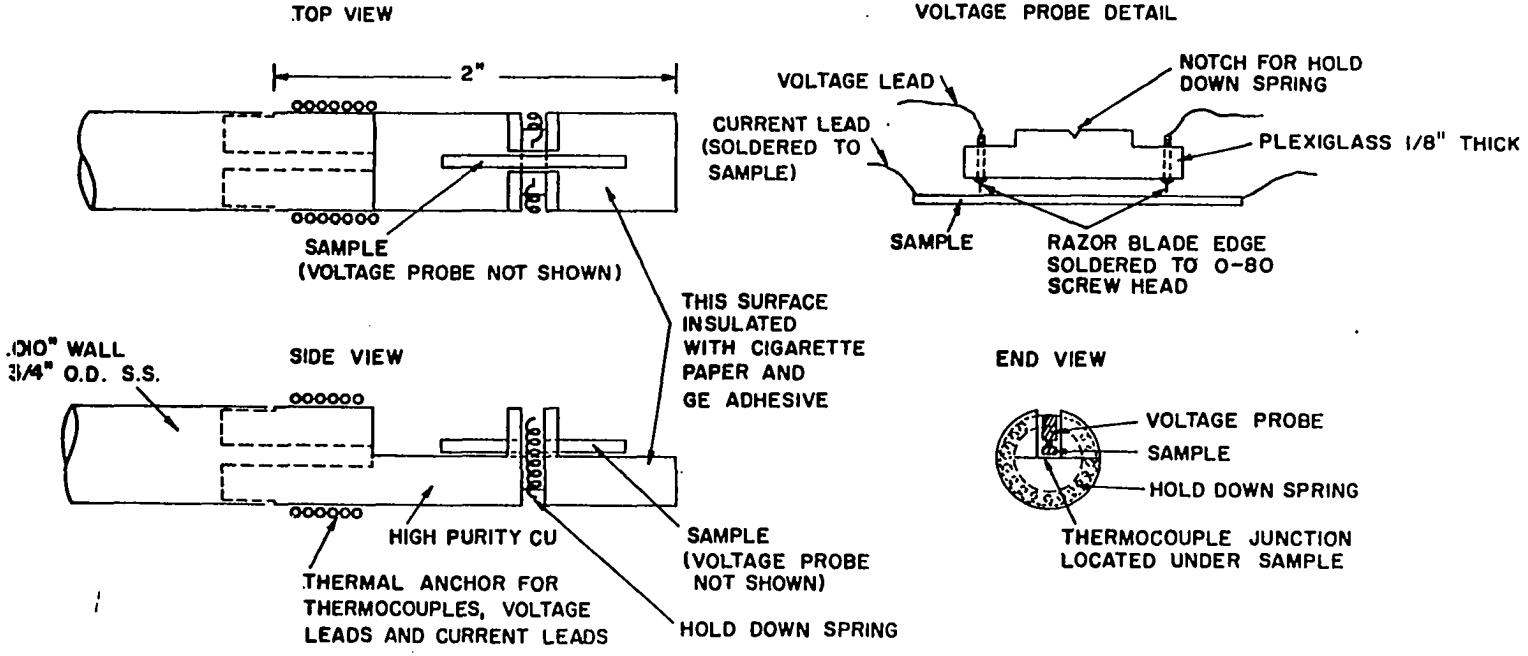

Figure 9. The sample holder for the electrical resistivity measurements

The AuFe wire had a composition of 0.03 at. % Fe and the roll from which it came was calibrated by W. Gray of this Laboratory who made a comparison with a calibrated germanium resistor. Because of inhomogenities in the wire, two thermocouples prepared from the same roll will differ by several microvolts at low temperatures. These thermocouple calibrations were corrected at the boiling points of liquid helium, hydrogen and nitrogen by a method described by Rhyne (40).

The thermocouple voltages were measured with a Leeds and Northrup type K-3 potentiometer and a Leeds and Northrup type 9834 null detector. The absolute accuracy of the temperature measurement is estimated to be $\pm$ 0.5°K while the relative accuracy is about 0.1°K over the range 1.3 to 300°K.

The dewar system and the heat leak chamber have been described by Colvin et al. (7). From 4.2 to 300°K the temperature of the sample was stabilized to within $\pm$ 0.1°K by automatically controlled heaters on the inside wall of the heat leak chamber. The automatic temperature control bridge, amplifier, and power supply have been described by Rhyne (40). Various cryogenic liquids were used to get the desired temperature range. Liquid helium was used from 4.2 to 25°K, liquid hydrogen was used from 20 to 80°K and liquid nitrogen was used from 77 to 300°K. For temperatures below 4.2°K, helium was condensed into the sample chamber and pumped on with a Welch model 1397 Duo-seal vacuum pump. The pressure over the liquid helium and hence the temperature was controlled by a manostat (41) between the vacuum pump and the sample chamber.

C. Measurement of the Seebeck Coefficients

If a metal has a temperature gradient, $\Delta T/L$, and is electrically insulated, a voltage per unit length, $\Delta V/L$, will be developed in a direction parallel to the temperature gradient and is related to $\Delta T/L$ by the following equation

$$\Delta V/L = S\Delta T/L \quad , \tag{3.2}$$

where S is the Seebeck coefficient. To measure the latter experimentally the basic thermoelectric circuit shown in Figure 10 is used. The open circuit potential difference, ΔV_{AX}, is given by

$$\Delta V_{AX} = -\oint \vec{E} \cdot d\vec{r} \quad ,$$

where $\vec{E}$ is an electric field and $d\vec{r}$ is an infinitesimal displacement along the circuit. From the definition of the Seebeck coefficient

$$\vec{E} = S\nabla T \quad , \tag{3.4}$$

Equation 3.3 becomes

$$\Delta V_{AX} = \int_{T_0}^{T+\Delta T} S_A dT + \int_{T+\Delta T}^{T} S_X dT + \int_{T}^{T_0} S_A dT \quad ,$$

and therefore

$$\Delta V_{AX} = \int_{T}^{T+\Delta T} (S_A - S_X) dT = \int_{T}^{T+\Delta T} S_{AX} dT \quad . \tag{3.5}$$

In the limit $\Delta T/T \ll 1$

$$\Delta V_{AX} = (S_A - S_X)\ \Delta T \quad . \tag{3.6}$$

Thus, only the difference in Seebeck coefficients can be measured. The

BASIC THERMOELECTRIC CIRCUIT
AND SIGN CONVENTION

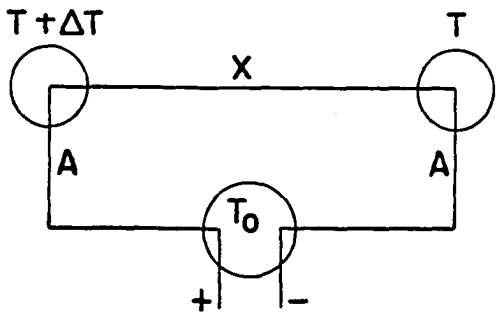

$$S_{AX} = \lim_{\Delta T \to 0} \frac{\Delta V_{AX}}{\Delta T} = S_A - S_X$$

BASIC MEASURING CIRCUIT

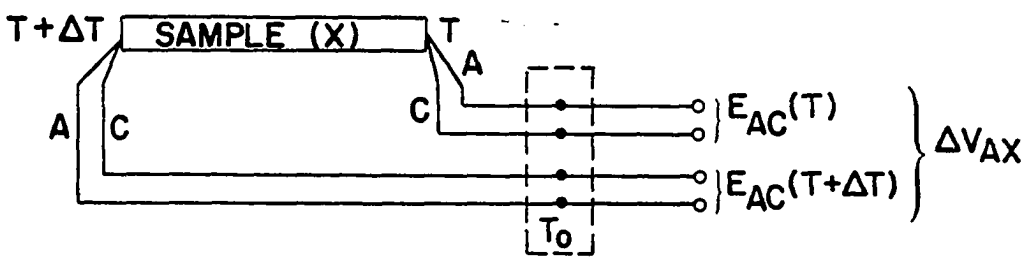

A = COPPER
C = CONSTANTAN OR AU-FE

$$\Delta E_{AC} = E_{AC}(T+\Delta T) - E_{AC}(T)$$

$$S_{AX} = \Delta V_{AX}\, S_{AC} / \Delta E_{AC}$$

Figure 10. The basic thermoelectric power circuit

Thomson heat, μ, and the Seebeck coefficient are related by one of the Kelvin relations (Equation 2.27)

$$S(T) = \int_0^T (\mu/T)\,dT \quad .$$

Borelius et al. (42) have measured the Thomson heat of lead and thus determined the absolute Seebeck coefficient. Since S = 0 for a superconductor, Christian et al. (43) have measured S for lead at low temperatures against Nb_3Sn. Hence, the circuit can be calibrated by replacing the sample (X) with lead.

The sample holder and heat leak chamber are shown in Figure 11. A description of the gradient heater, main heater, and the temperature control sensing elements is given by Sill (33) and Trego (44). The electronics for the automatic temperature control and the dewar system are the same as used in the resistivity measurements.

After the samples were run in the resistivity apparatus, they were electropolished again and retinned with indium before they were soldered into this sample holder. The absolute temperature and temperature gradient were measured with Cu versus constantan and Cu versus AuFe (0.03 at. % Fe) thermocouples. The thermocouple junctions were soldered to the ends of the sample to insure good thermal contact.

The basic thermoelectric measuring circuit is shown in Figure 10. If there is a temperature difference, ΔT, then

$$\Delta V_{AX} = S_{AX}\Delta T + e_1 \quad , \tag{3.5}$$

$$\Delta E_{AC} = S_{AC}\Delta T + e_2 \quad , \tag{3.6}$$

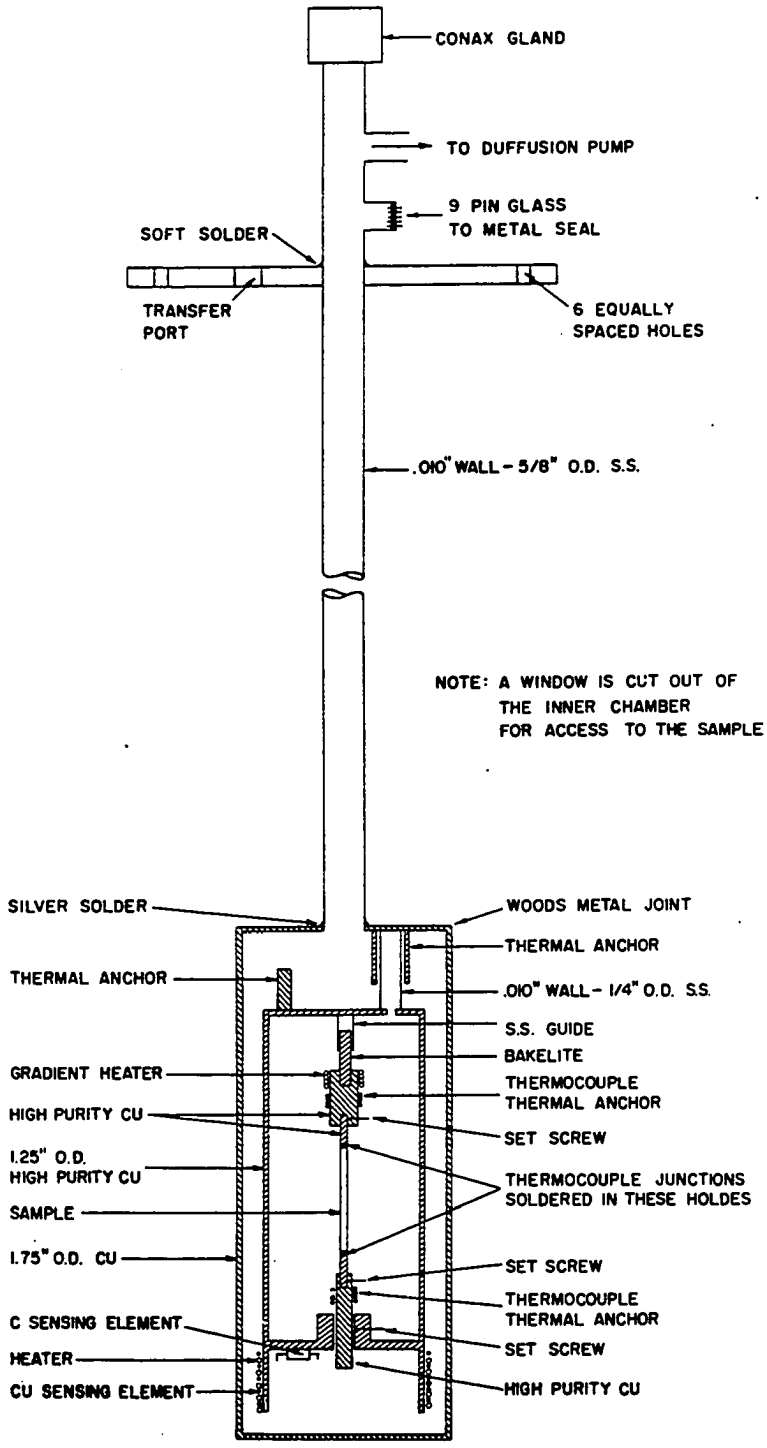

Figure 11. The sample holder and heat leak chamber for the Seebeck coefficient measurements.

where ΔE_{AC} is the net voltage difference between the hot and cold thermocouples, S_{AC} is the sensitivity of the thermocouples at the average temperature of the sample, and e_1 and e_2 are extraneous voltages caused by thermals in the circuit. To keep e_1 and e_2 small the thermocouple and voltage leads are insulated with teflon tubing and are run continuously to the ice bath. Experimentally, it was found that when $\Delta T = 0$, e_1 was a function of temperature but remained approximately the same function for various samples (X) in the circuit. For a lead sample and a thulium sample, Equation 3.5 becomes

$$\Delta V_{ATm} = S_{ATm}\Delta T_1 + e_1 \quad ,$$

$$\Delta V_{APb} = S_{APb}\Delta T_2 + e_1 \quad ,$$

and

$$\Delta V_{ATm} - \Delta V_{APb} = S_{Pb}\Delta T_2 - S_{Tm}\Delta T_1 \quad . \tag{3.8}$$

Thus if the temperature gradient is kept approximately constant for all samples, e_1 will be virtually eliminated. If e_1 and e_2 are assumed to be negligible, then Equations 3.5 and 3.6 become

$$S_X = S_A - \Delta V_{AX} S_{AC}/\Delta E_{AC} \quad . \tag{3.9}$$

Since $E_{AC}(T)$ and $E_{AC}(T+\Delta T)$ are generally large but nearly equal numbers, ideally these numbers should be subtracted electrically to eliminate gross errors in ΔE_{AC}. However, since the thermocouples are soldered to the ends of the sample this can not be done in a straight forward manner. A Dauphinee comparator circuit (33) shown in Figure 12 was used to obtain

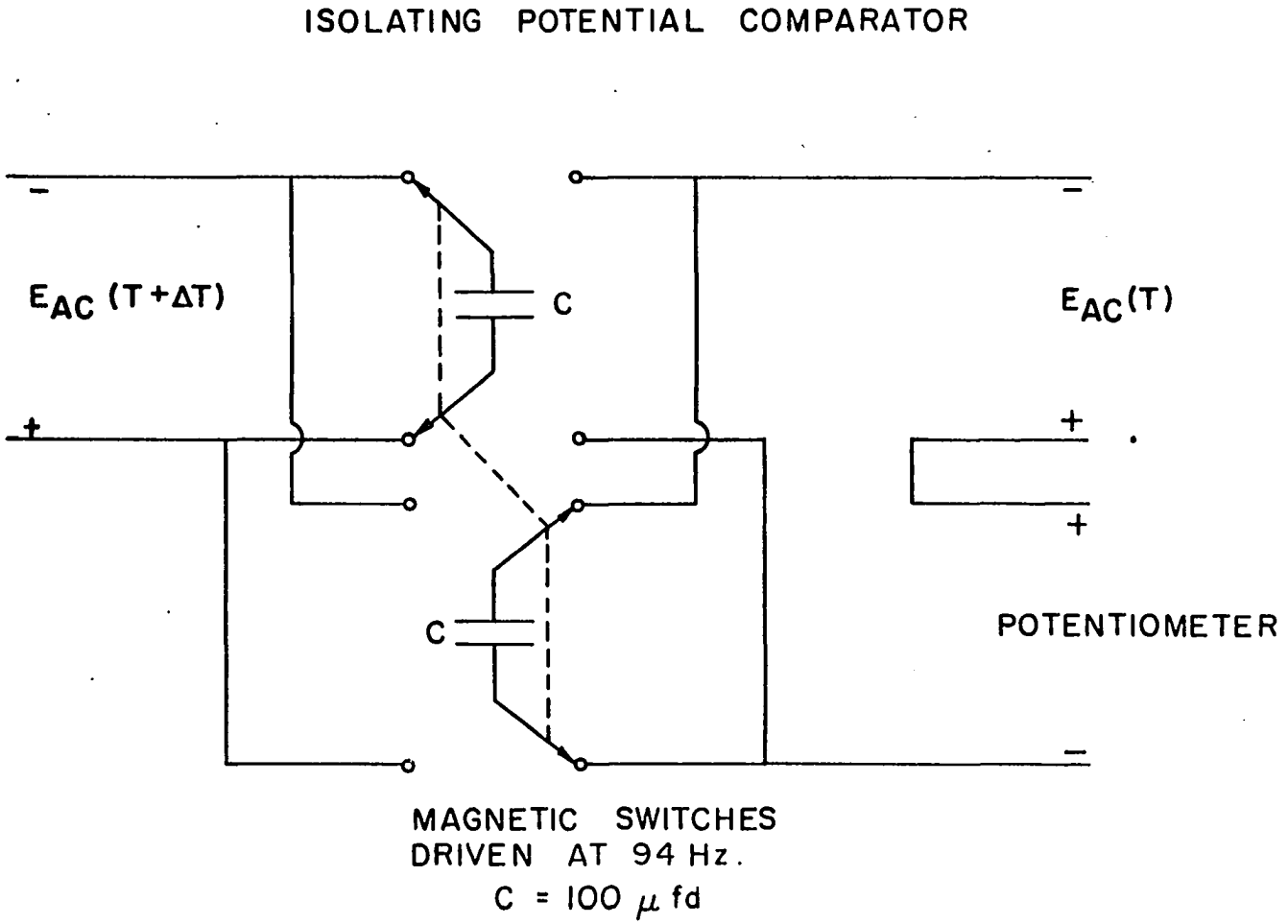

Figure 12. The Dauphinee potential comparator circuit

ΔE_{AC} directly. The complete thermoelectric circuit used in this experiment is shown in Figure 13. The voltages ΔE_{AC} and ΔV_{AX} were measured to a resolution of 0.01 microvolts with the Honeywell potentiometer system used in the resistivity measurements. The absolute temperature was measured with a Leeds and Northrup type K-3 potentiometer and 9834 null detector.

The emf versus temperature curves for these thermocouples were obtained by the same method used in the previous section. However, it was also necessary to differentiate these curves to obtain the sensitivities, S_{AC}. The Cu versus constantan curve was differentiated on the computer, but the Cu versus AuFe curve was done graphically because of rapid changes in curvature. Because of inhomogeneities in the thermocouple wires, $\Delta E_{AC} \neq 0$ when $\Delta T = 0$. To correct for this effect ΔE_{AC} was measured as a function of temperature with $\Delta T = 0$ for both the Cu versus constantan and Cu versus AuFe thermocouples.

The relative Seebeck coefficient between the Cu wires and a sample of 99.999% pure lead (obtained from American Smelting and Refining Corporation) was measured. The absolute Seebeck coefficient data of Christian et al. (43) for lead was then used to obtain the absolute Seebeck coefficient of the Cu leads. Thus from Equation 3.9 the absolute Seebeck coefficient of thulium was obtained.

Because both the Cu versus constantan and Cu versus AuFe thermocouples had very low sensitivities in the 20 to 30°K range, the Seebeck coefficient was obtained by the weighted average

$$S = [(30-T)\ S_{AuFe} + (T-20)\ S_{Con}]/10 \quad , \tag{3.10}$$

where S_{AuFe} is the Seebeck coefficient determined by the AuFe thermocouple

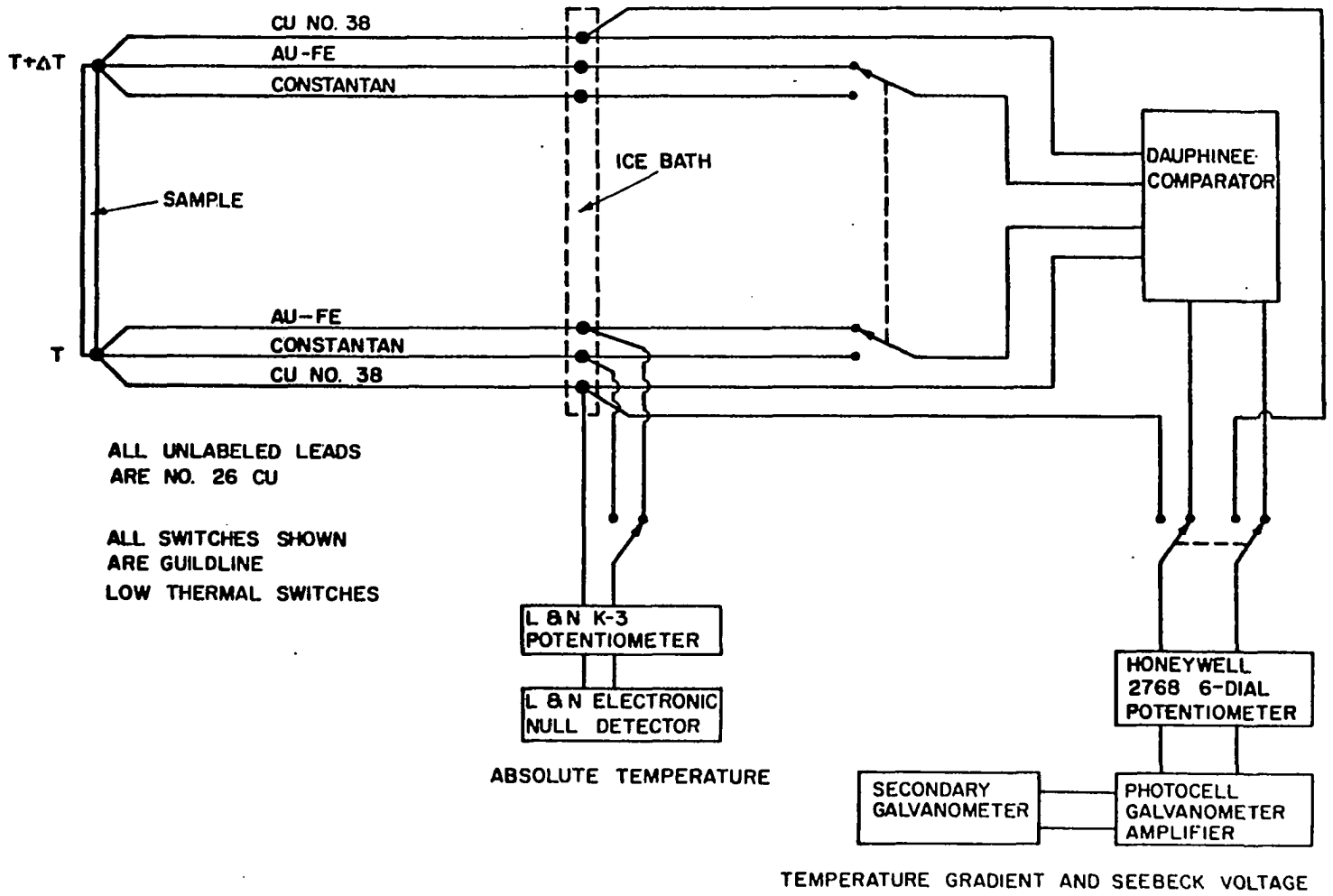

Figure 13. The complete circuit for measuring the Seebeck coefficient

and S_{Con} is the Seebeck coefficient determined by the constantan thermocouple.

All measurements were taken by the steady state heat flow method. Also because the rare earths absorb helium at low temperatures all measurements were made with a vacuum of 1×10^{-5} torr in the vacuum chamber.

D. Measurement of the Thermal Conductivity

If a metal of cross-sectional area, A, and length, L, has a temperature gradient, $\Delta T/L$, and is electrically insulated, an energy flux, $\dot{Q}/A$, will be developed in a direction parallel to the temperature gradient. The energy flux is related to the temperature gradient by the following equation

$$\dot{Q}/A = K\Delta T/L \quad , \tag{3.11}$$

where K is the thermal conductivity.

The thermal conductivity was measured by the steady state heat flow method with corrections for radiation and conduction heat losses.

The apparatus used to measure the thermal conductivity of thulium was designed and constructed by D. W. Boys (45) and is described in detail in his Ph.D. dissertation.

IV. RESULTS

A. Electrical Resistivity

The electrical resistivity of thulium in the three crystallographic directions was measured as a function of temperature from 1.3 to 300°K. The results of these measurements are shown in Figure 14. The residual resistivities have not been subtracted out. Because ρ_a and ρ_b are identical, only ρ_a is shown for clarity.

With decreasing temperature ρ_c decreases linearly down to 57.5°K, increases rapidly at 57.5°K, goes through a maximum, and then decreases smoothly to the residual level. The 57.5°K transition is in agreement with the neutron diffraction results of Koehler et al. (19). They found a Néel temperature of 56°K. The basal plane resistivity does not exhibit a maximum, but only goes through a change of slope at the Néel temperature. No anomalies are observed in the 30 to 40°K range for either crystallographic direction.

Alstad et al. (46) show that the polycrystalline resistivity, ρ_{poly}, is given by

$$\rho_{poly} = 1/3\rho_c + 2/3\rho_a \quad . \tag{4.1}$$

ρ_{poly} calculated from the single crystal data of this study and the experimental polycrystalline resistivity of Colvin et al. (7) are shown in Figure 15. The experimental curve shows a more pronounced maximum and is lower in absolute magnitude. This discrepancy would be understandable if in Colvin's polycrystalline sample the small crystallites showed a preferential orientation of the c-axis parallel to the long direction of the sample.

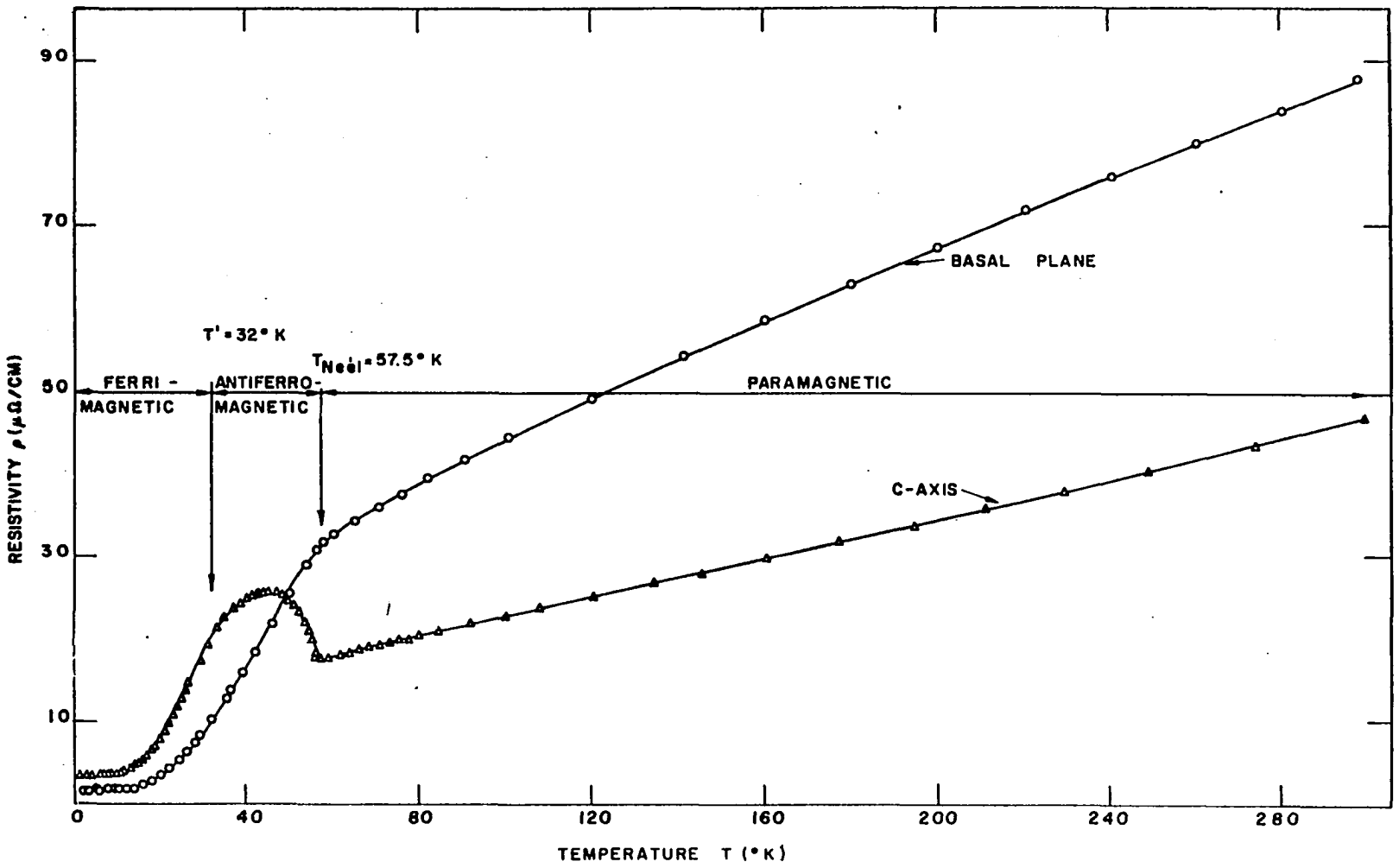

Figure 14. The electrical resistivity as a function of temperature for the basal plane and c-axis thulium crystals

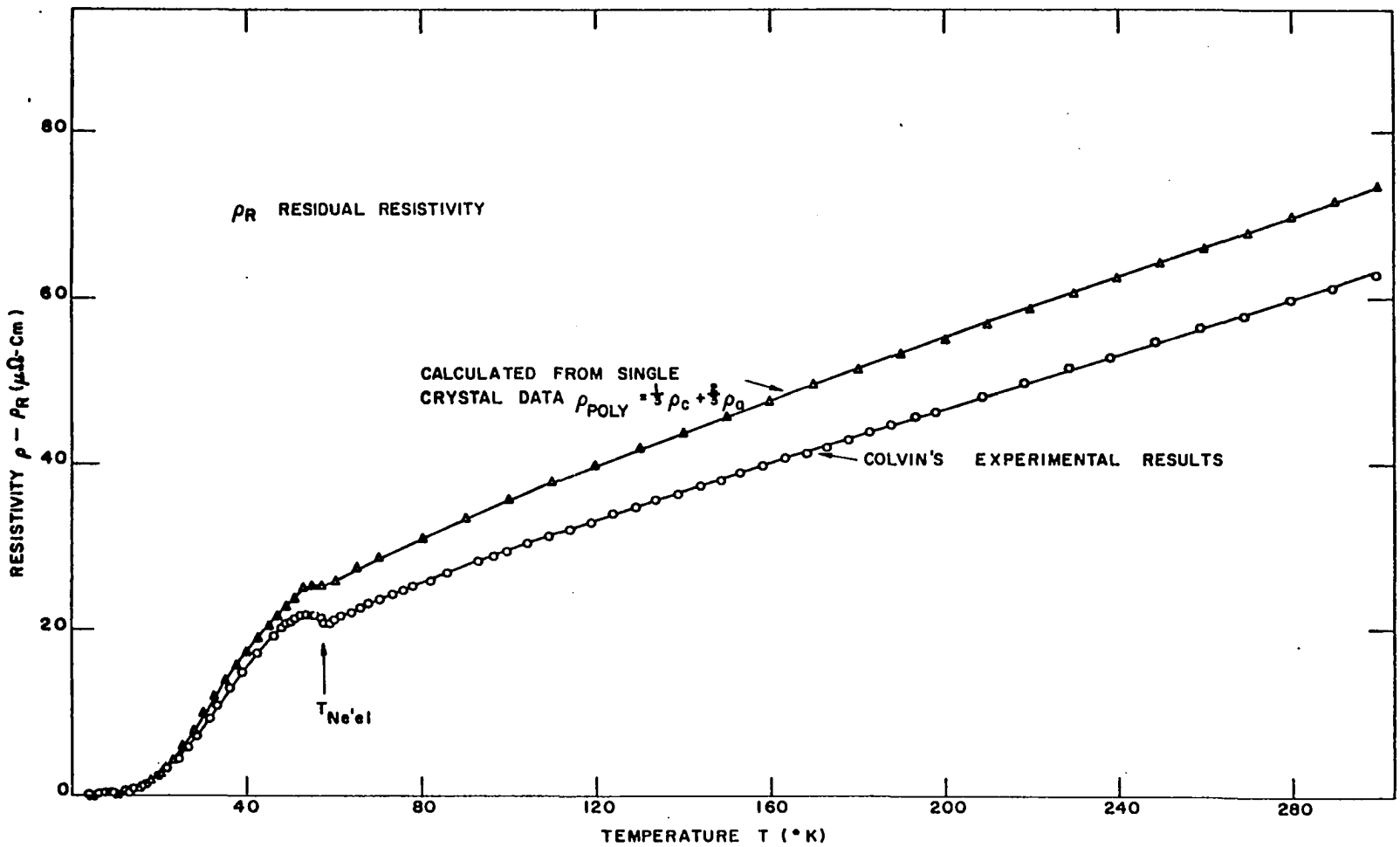

Figure 15. The experimental and calculated electrical resistivity as a function of temperature for polycrystalline thulium

B. Seebeck Coefficients

The thermoelectric power of thulium for the three crystallographic directions was measured as a function of temperature from 7 to 300°K. The results are shown in Figure 16. Because the Seebeck coefficients are more sensitive to impurity scattering than the other transport properties both S_a and S_b are shown. The b-axis crystal is of higher purity than the a-axis crystal, and the effects of the impurities is quite evident below 20°K.

Both S_a and S_b exhibit sharp maxima at 57.5°K, while S_c has a sharp maximum at 55°K. This is in good agreement with the Néel temperature determined by Koehler et al. (19) and the resistivity measurements of this study. The a and b-axis coefficients have no other anomalies, but the c-axis coefficient has a sharp minimum at 32°K. This is in agreement with the results of Jelinek et al. (17), who observe a sharp peak at 30°K in the A. C. susceptibility of polycrystalline thulium. The neutron diffraction data of Koehler et al. (19), however, indicate that the ferrimagnetic-antiferromagnetic transition should be approximately 38°K.

C. Thermal Conductivity

The thermal conductivity of thulium in the b and c crystallographic directions was measured as a function of temperature from 5 to 300°K. The results are shown in Figure 17. Both K_c and K_b exhibit highly peaked maxima at low temperatures which is characteristic of high purity metals.

With increasing temperature the slope of K_c decreases sharply at 58°K, while the slope of K_b changes sign at 56.5°K. These transition temperatures are in agreement within experimental error with the other transport

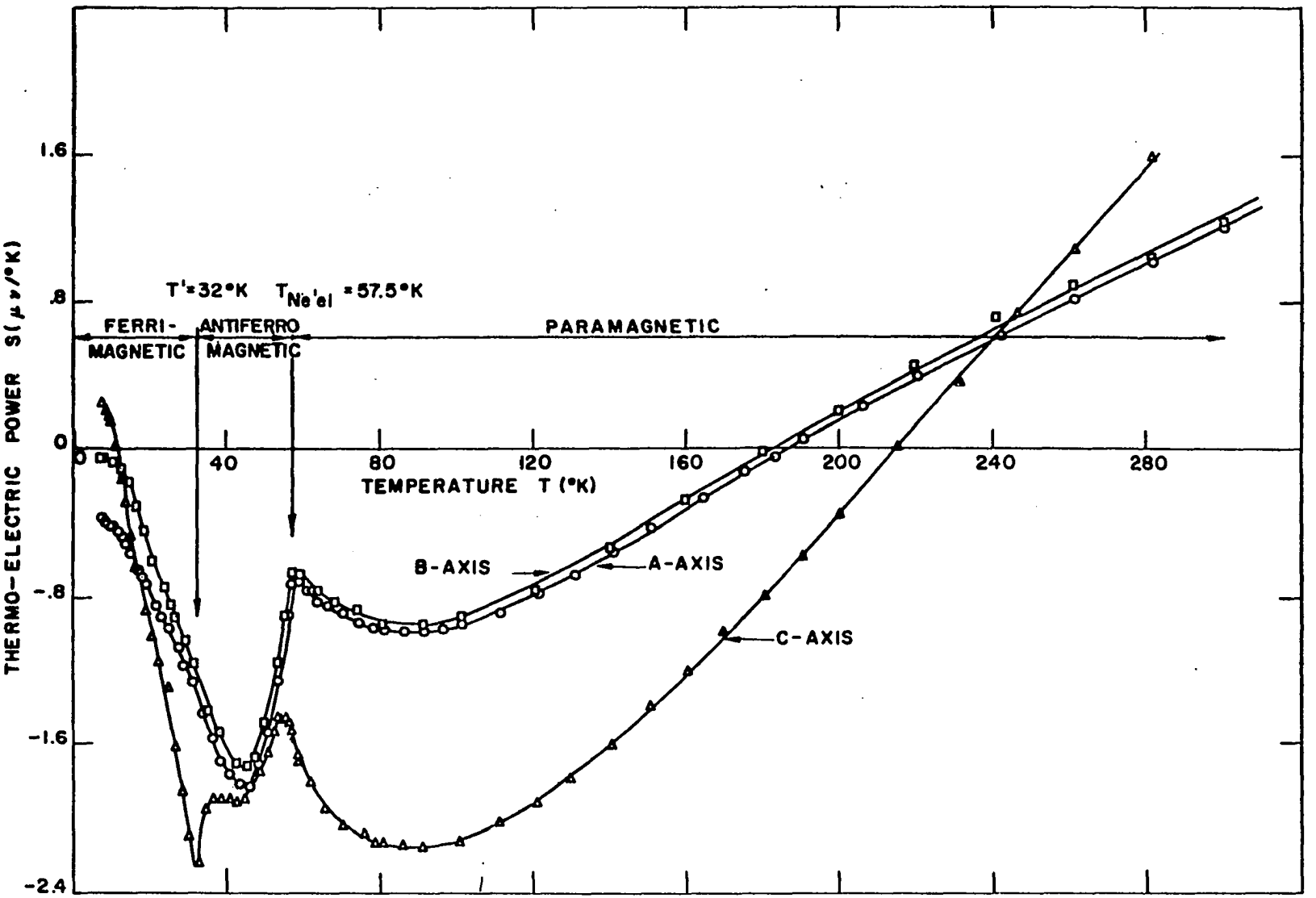

Figure 16. The Seebeck coefficient as a function of temperature for the a, b, and c-axis thulium crystals

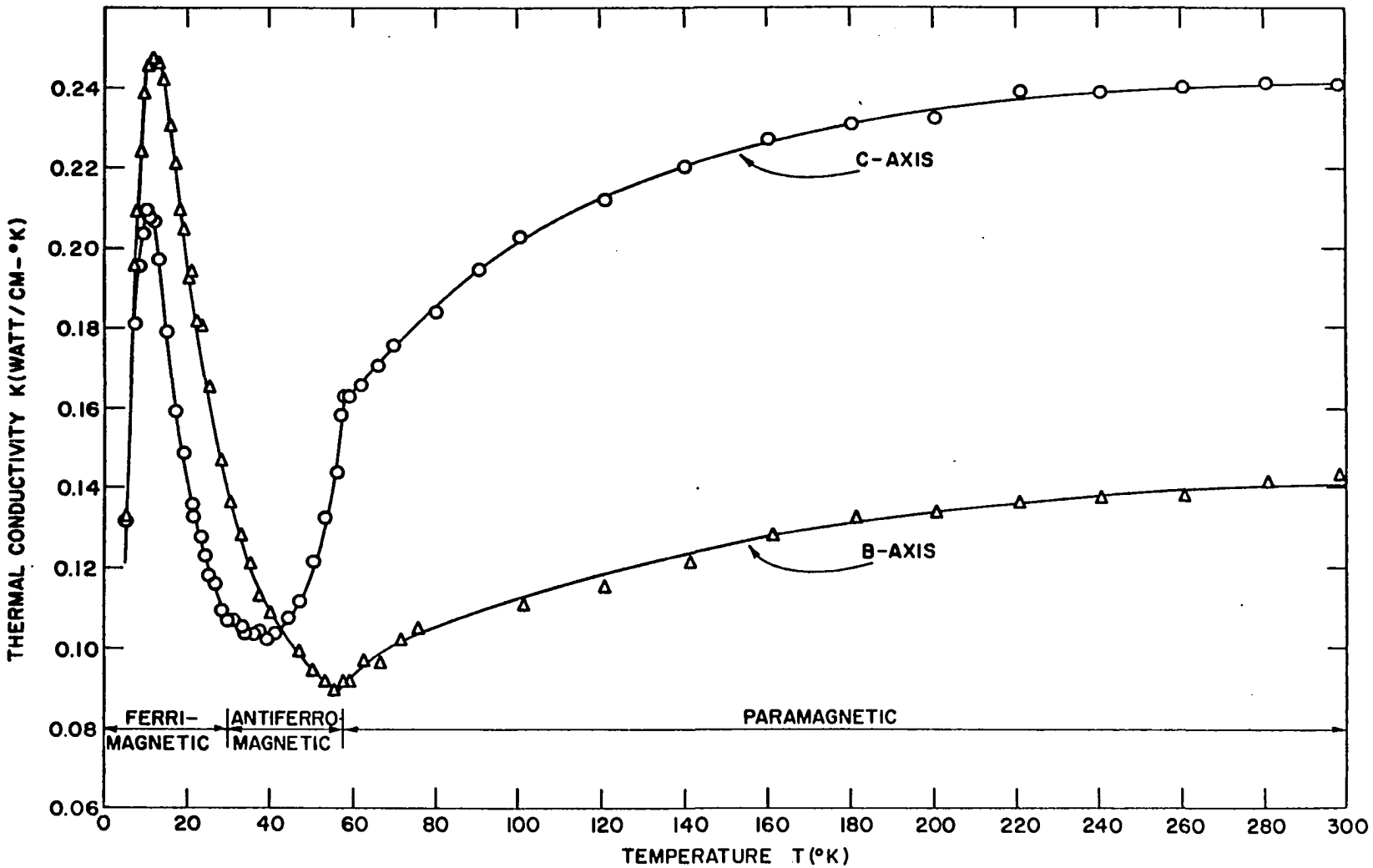

Figure 17. The thermal conductivity as a function of temperature for the b and c-axis thulium crystals

properties. There are no other anomalies observed in K_b, but K_c has a small anomaly at $30^{o}K$ which is in agreement with the anomaly observed in the c-axis Seebeck coefficient.

The Lorenz function for the b and c crystallographic directions was calculated from Equation 2.60 and plotted as a function of temperature. The results are shown in Figure 18. At high temperatures ($T > \theta_D$, $\theta_D = 167^{o}K$) the Lorenz functions are nearly independent of temperature, while at low temperatures they are very dependent on temperature. Both functions exhibit anomalies at $57^{o}K$.

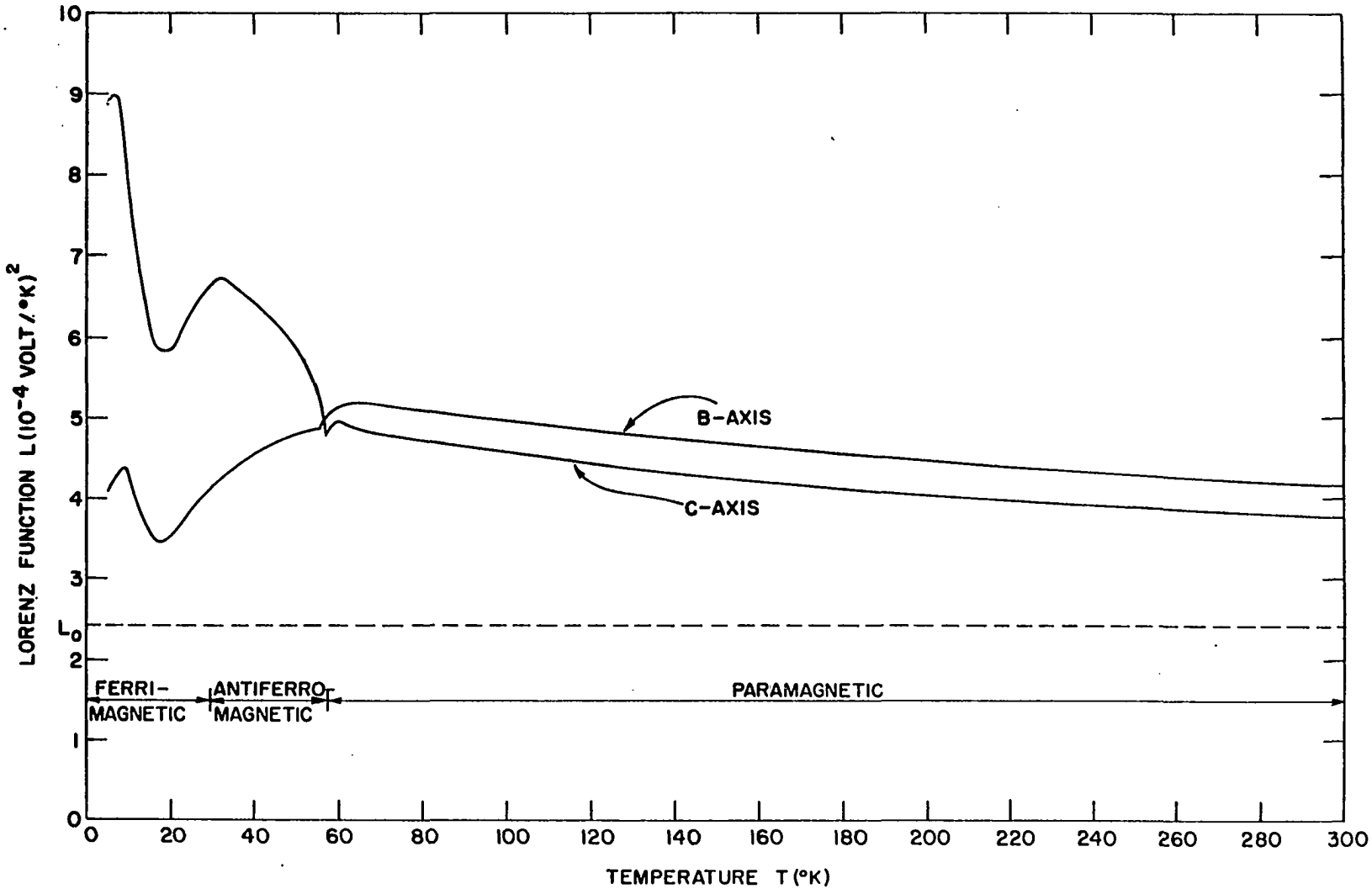

Figure 18. The Lorenz function as a function of temperature for the b and c-axis thulium crystals

V. DISCUSSION

The theory of magnetic superzones has been one of the most significant developments toward understanding the anomalous behavior of the conduction electrons in the heavy rare earths. Mackintosh (28) and Elliott and Wedgewood (26) have explained qualitatively the anomalies observed in the resistivities of terbium, holmium, dysprosium, and erbium around the magnetic transitions. Freeman et al. (27) predict on the basis of their calculated Fermi surface for thulium and a second order perturbation calculation of the positions of the superzone planes, that ρ_c will increase sharply at the Néel temperature and go through a maximum, while ρ_a and ρ_b will just decrease more rapidly below the Néel temperature. The experimental results for thulium are in good agreement with this prediction.

Below the Néel temperature the moments lie along the hexagonal axis and the amplitude of the moments is sinusoidally modulated. This magnetic structure (cf. Equation 2.8) can be described analytically by

$$\langle J_n^X \rangle = \langle J_n^Y \rangle = 0 \quad , \tag{5.1a}$$

$$\langle J_n^Z \rangle = MJ \cos (\vec{q}\cdot\vec{R}_n) \quad . \tag{5.1b}$$

If the magnetic structure is described by the above equations, then from Equations 2.15 the electrical resistivity of thulium is given by the following phenomonological expressions

$$\rho_a = \alpha_1 + \beta_1 T + \gamma_1 (1 - 1/2\, M^2) \quad , \tag{5.2a}$$

$$\rho_c = \frac{\alpha_2 + \beta_2 T + \gamma_2 (1 - 1/2\, M^2)}{1 - \Gamma M} \quad , \tag{5.2b}$$

where α, β, γ are obtained from the experimental data as described in Section II. M is the reduced moment per atom and its temperature dependence is deduced from the neutron diffraction data for thulium (19). The temperature dependence of M and M^2 is shown in Figure 19. A comparison between the resistivities as calculated from Equations 5.2 and the experimental resistivities is shown in Figures 20 and 21. $\Gamma = .86$ gave the best fit for ρ_c, however, Elliott and Wedgewood (26) had predicted a value of $\Gamma = .29$ for thulium. Since $\sum_i |\ell_i|$, where ℓ_i is the position vector of the superzone planes (cf. Equation 2.15), the number of superzone planes will greatly affect the value of Γ. On the basis of first order perturbation theory, Elliott and Wedgewood predict only four superzones, while Freeman et al. (27) using second order perturbation theory predict eight planes. To a first approximation this will effectively double Γ. The poor fit at low temperature is probably due to the assumption of linear temperature dependence for phonon scattering, the neglect of spin wave scattering, and the assumption that the magnetic structure is represented by a sine wave. The squaring of the magnetic structure will be discussed in more detail later. Mackintosh (cf. Equation 2.16) suggests a $T^2 \exp(-\epsilon/kT)$ dependence for the spin wave scattering resistivity at low temperatures, which would have the effect of pulling the theoretical curve closer to the experimental curve. Since the Fermi surface of thulium is anything but ellipsoidal, a detailed agreement between theory and experiment can not be expected, however, the theory is successful in that it does predict on a semiquantitative basis the anomaly at the Néel temperature.

Above the Néel temperature, the resistivity is almost linear with temperature and the spin disorder resistivity, ρ_{sd}, is obtained by a linear

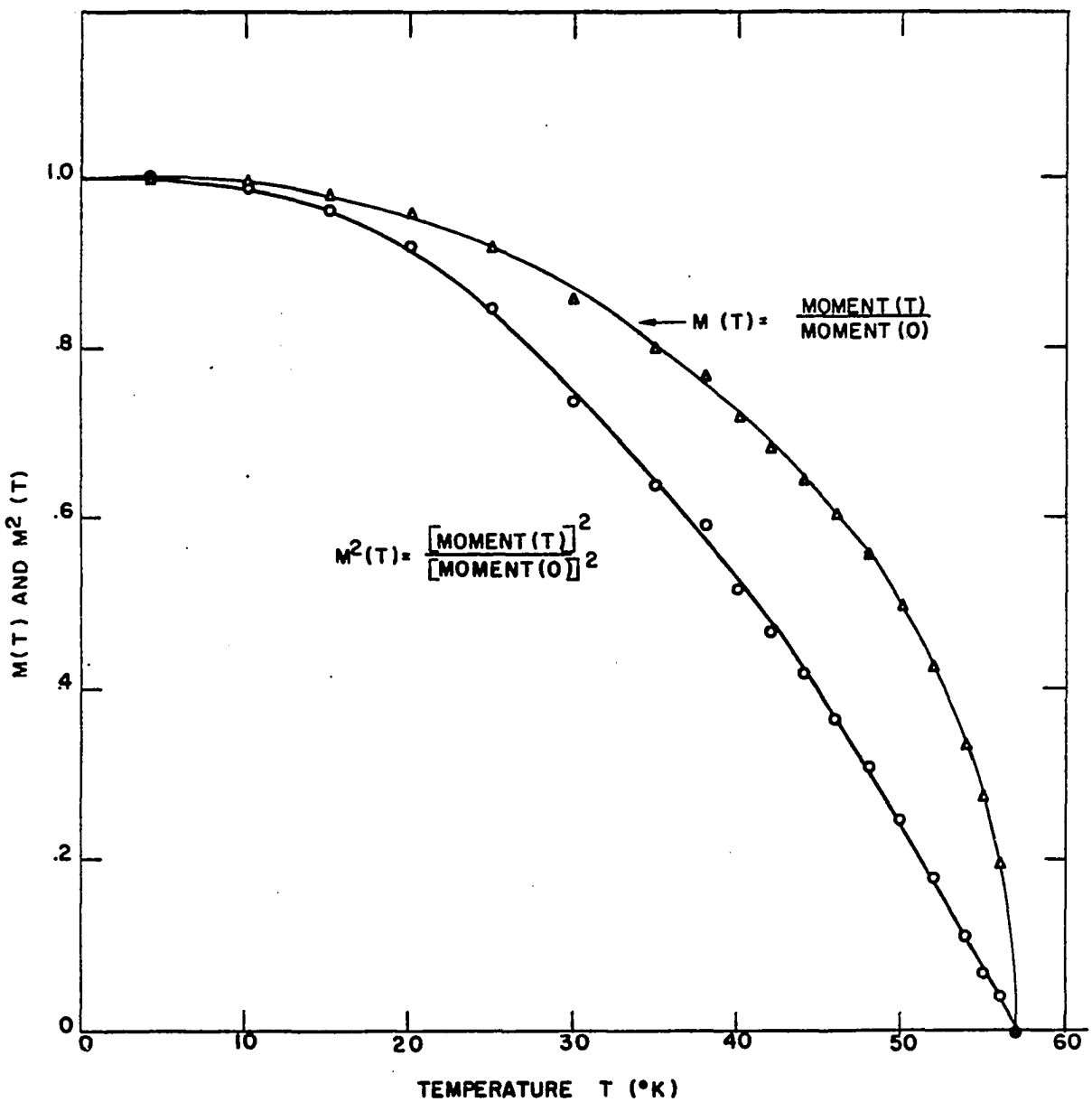

Figure 19. The reduced moment per atom and the reduced moment per atom squared as a function of temperature for thulium

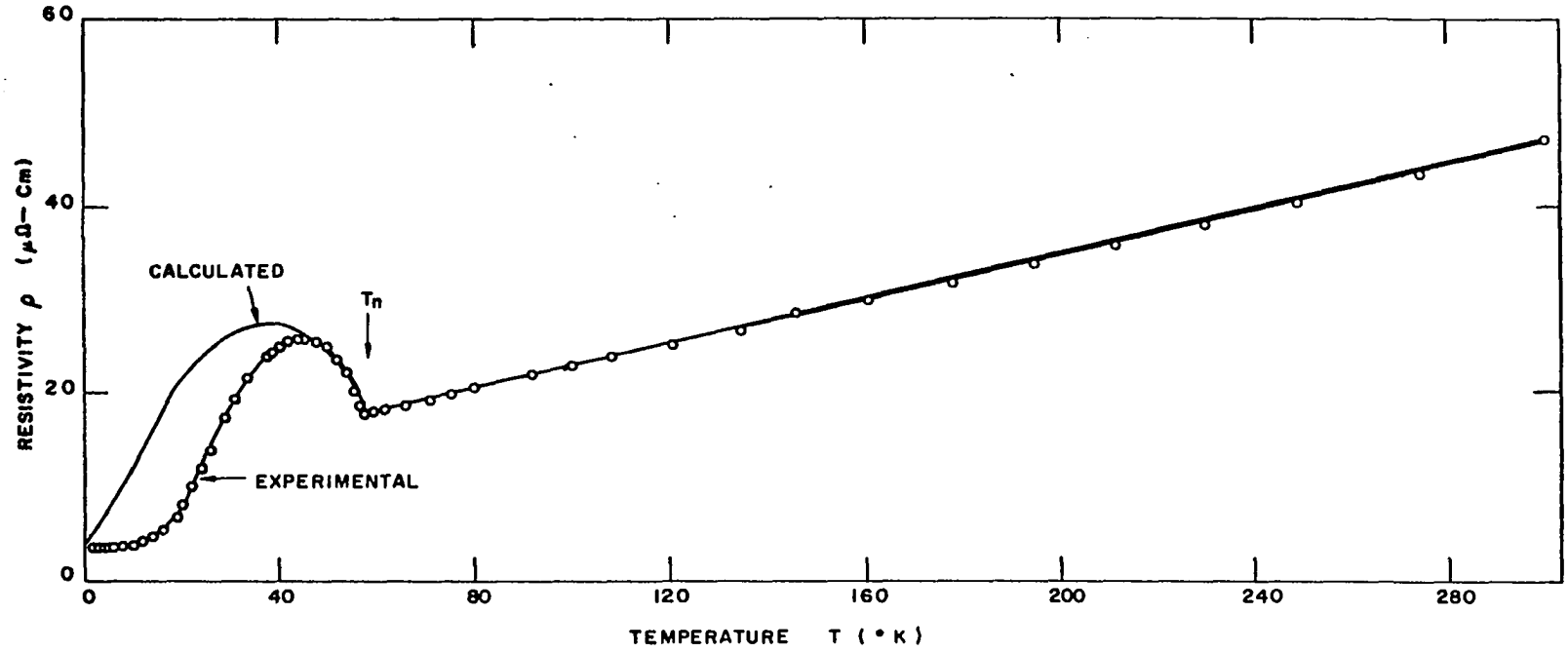

Figure 20. The calculated and experimental electrical resistivity as a function of temperature for the c-axis thulium crystal

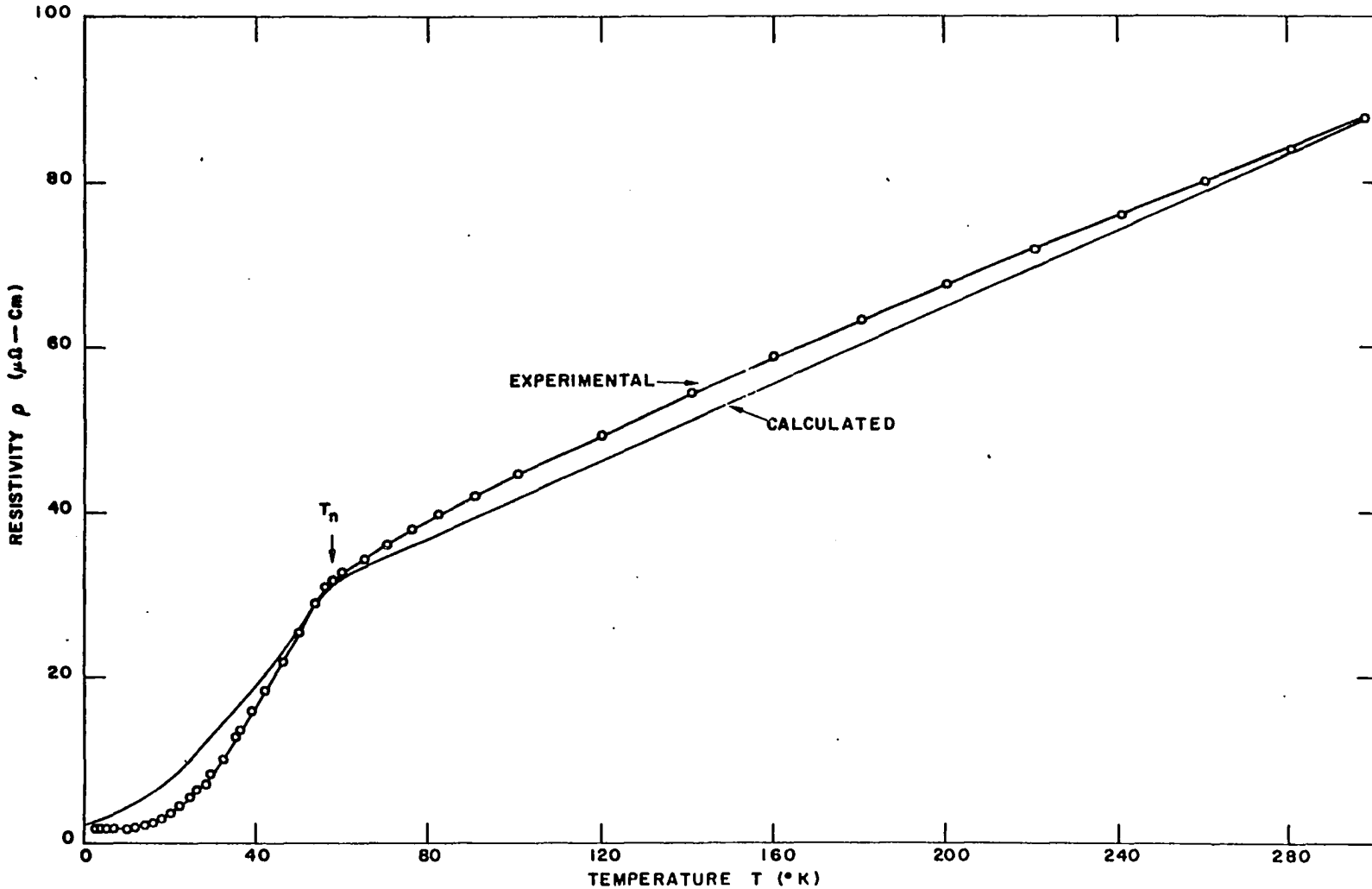

Figure 21. The calculated and experimental electrical resistivity as a function of temperature for the a-axis thulium crystal

extrapolation of the high temperature resistivity to zero temperature. It is found that $\rho^a_{s\sim} = 22.3\ \mu\Omega$ - cm, $\rho^c_{s\sim} = 7.4\ \mu\Omega$ - cm, and the high temperature slope of ρ_a is greater than that of ρ_c. These observations can be explained by the anisotropy of the Fermi surface. The conductivities for the a and c directions are obtained from Equation 2.1.

$$\sigma_a = (e^2/4\pi^3\hbar) \int_{E_F} \tau v_x d\mathcal{S}_x \quad , \tag{5.3a}$$

$$\sigma_c = (e^2/4\pi^3\hbar) \int_{E_F} \tau v_z d\mathcal{S}_z \quad . \tag{5.3b}$$

If impurity scattering is neglected, and if the sample temperature is above the Néel temperature, the relaxation time is given by

$$1/\tau = \beta T + 1/\tau_S \quad , \tag{5.4}$$

where $(\beta T)^{-1}$ is the relaxation time for phonon scattering and $1/\tau_S$ is the relaxation time for spin disorder scattering. τ_S is independent of temperature for magnetic disorder scattering (cf. Equation 2.17). If $v_x \sim v_z \sim \bar{v}$, then Equations 5.3 become

$$\rho_a = 1/\sigma_a = (4\pi^3\hbar/e^2)(1/\tau)\left(\int_{E_F} d\mathcal{S}_x\right)^{-1} \quad ,$$

$$\rho_c = 1/\sigma_c = (4\pi^3\hbar/e^2)(1/\tau)\left(\int_{E_F} d\mathcal{S}_z\right)^{-1} \quad .$$

Use of Equation 5.4 for $1/\tau$ then yields

$$\rho_a = (4\pi^3\hbar/e^2)\left[\frac{T}{\bar{v}\int_{E_F} d\mathcal{S}_x} + \frac{1}{v\tau_S \int_{E_F} d\mathcal{S}_x}\right] \quad , \tag{5.5a}$$

$$\rho_c = (4\pi^3\hbar/e^2)\left[\frac{T}{\bar{v}\int_{E_F} d\ell_z} + \frac{1}{\bar{v}\tau_s\int_{E_F} d\ell_z}\right] \quad . \tag{5.5b}$$

These equations are linear in T and are in the form

$$\rho_a = (d\rho_a/dT)\ T + \rho^a_{s\sim} \quad , \tag{5.6a}$$

$$\rho_c = (d\rho_c/dT)\ T + \rho^c_{s\sim} \quad . \tag{5.6b}$$

From Figure 1 the projected area of the Fermi surface in the c direction is greater than the projected area in the basal plane direction, i.e.

$$\int_{E_F} d\ell_z > \int_{E_F} d\ell_x \quad . \tag{5.7}$$

Hence, from Equation 5.5, 5.6 and 5.7 the following results are obtained

$$(d\rho_a/dT) > (d\rho_c/dT) \quad , \tag{5.8a}$$

$$\rho^a_{s\sim} > \rho^c_{s\sim} \quad , \tag{5.8b}$$

which is in agreement with experiment. This result is also verified for gadolinium, terbium, dysprosium, holmium, erbium, and yttrium. This is not surprising since all these elements have similar high temperature Fermi surfaces (47). Thus, even through the assumption $v_x \sim v_z \sim \bar{v}$ is quite crude, the fact that Equations 5.8 predict the correct behavior for all the heavy rare earths leads one to conclude that the Fermi surface anisotropy is responsible for the anisotropies observed in the resistivities. It is unfortunate that the band structure calculations for thulium are not available for it would be interesting to make a numerical evaluation of Equations 5.3.

The thermal conductivity will be discussed next because of its relationship to the electrical resistivity through the Wiedemann-Franz law.

From Figure 17 the thermal conductivities of both crystallographic directions are constant at room temperature. This is typical of most metals and is also an indication that the radiation corrections were quite good.

One of the most striking features is the large anisotropy in the thermal conductivity above the Néel temperature. Above the Debye temperature ($167^{\circ}K$) the Lorenz function, L. for both axes is a slowly varying function of temperature and becomes nearly independent of temperature at $300^{\circ}K$ (cf. Figure 18). Thus, the electron scattering is elastic at room temperatures and the Wiedemann-Franz law holds. Hence, the ratio of K_b to K_c is given by

$$K_c/K_b = \rho_b/\rho_c \quad , \tag{5.9}$$

and from Equation 5.8b

$$K_c > K_b \quad . \tag{5.10}$$

This is in agreement with experimental results. Therefore, the anisotropy in the high temperature thermal conductivity is due to the anisotropy of the Fermi surface.

At room temperature the electronic thermal conductivity, K_E, can be determined from the Wiedemann-Franz law (Equation 2.59) and a knowledge of the electrical resistivity. The results at $300^{\circ}K$ are

$$(K_E)_b = L_o T/\rho_b = .084 \text{ watt/cm}^{\circ}K \quad ,$$

$$(K_E)_c = L_o T/\rho_c = .156 \text{ watt/cm}^{\circ}K \quad .$$

Thus from Equation 2.42 the lattice thermal conductivity plus the magnon

thermal conductivity, $K_L + K_M$, can be determined with the above results for K_E to get

$$(K_L + K_M)_b = .066 \text{ watt/cm}^\circ\text{K} \quad ,$$

$$(K_L + K_M)_c = .094 \text{ watt/cm}^\circ\text{K} \quad .$$

Presently there is no way of separating K_L and K_M.

At about 16°K both K_c and K_b exhibit sharp maxima which are typical of relatively pure metals. If electron-impurity and electron-phonon interactions give rise to the dominant scattering mechanisms, then from Equation 2.60

$$T/K_b = A_b + B_b T^3 \quad , \tag{5.11a}$$

$$T/K_c = A_c + B_c T^3 \quad , \tag{5.11b}$$

where A is the electron-impurity scattering constant and B is the electron-phonon scattering constant. Plots of T/K versus T^3 for both crystallographic directions are shown in Figure 22. The plots are linear up to 20°K which indicates that the electrons are the dominant carriers and that electron-impurity and electron-phonon scattering are the dominant mechanisms. The following values were obtained for the constants

$$A_b = 34.2 \ (^\circ\text{K})^2 \text{ cm/watt}$$

$$A_c = 35.8 \ (^\circ\text{K})^2 \text{ cm/watt}$$

$$B_b = 8.4 \times 10^{-3} \text{ cm/watt} - {}^\circ\text{K}$$

$$B_c = 13.1 \times 10^{-3} \text{ cm/watt} - {}^\circ\text{K} \quad .$$

Now at low temperatures Equations 5.11 become

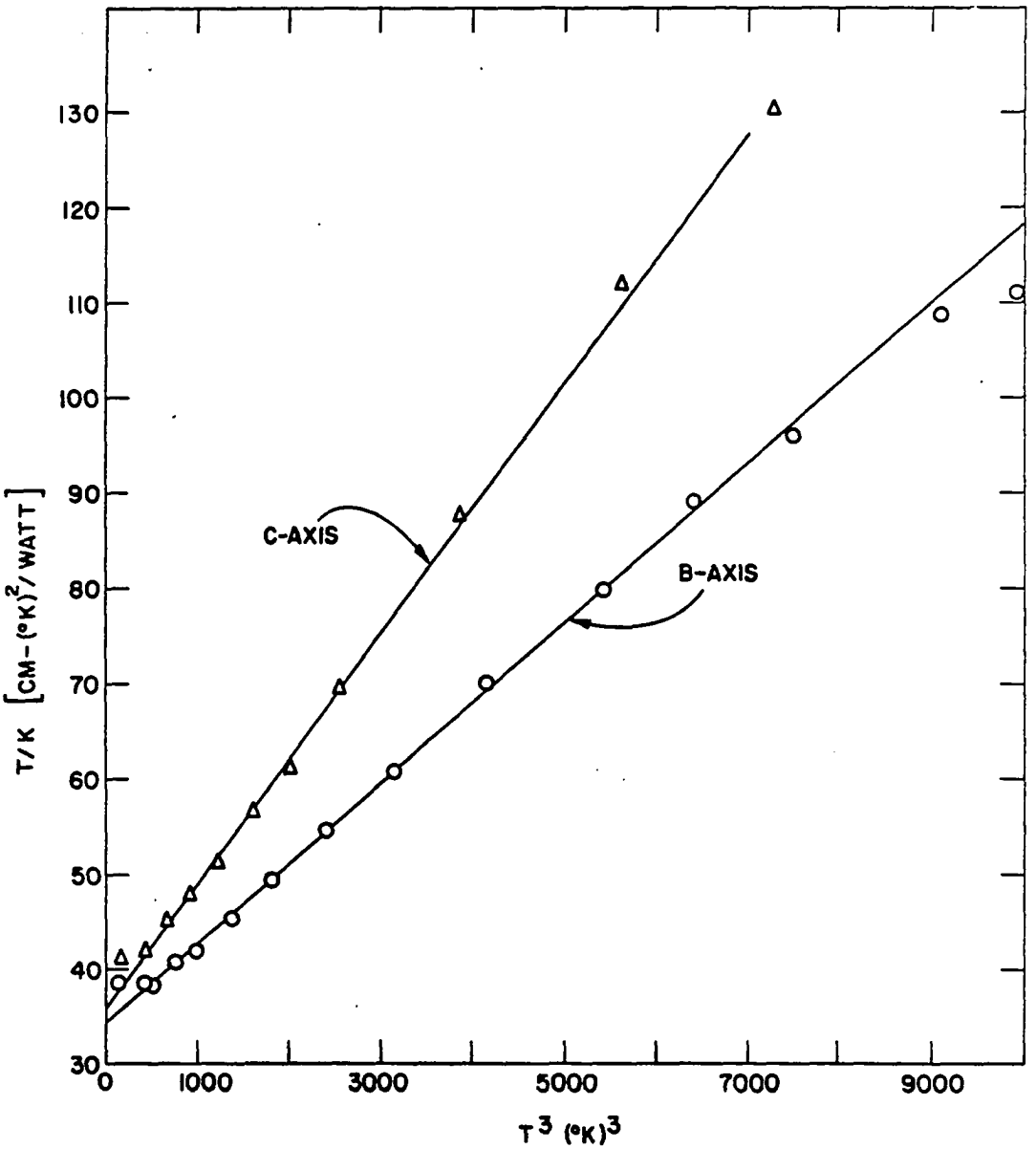

Figure 22. T/K as a function of T^3 for the b and c-axis thulium crystals

$$T/K_b = A_b \quad , \tag{5.12a}$$

$$T/K_c = A_c \quad . \tag{5.12b}$$

Since electron-impurity scattering is elastic, the Wiedemann-Franz law holds and

$$K_b = L_o T/\rho_b^o \quad , \tag{5.13a}$$

$$K_c = L_o T/\rho_c^o \quad , \tag{5.13b}$$

where ρ_b^o and ρ_c^o are the residual resistivities. Thus, the constant A_b and A_c are related to the residual resistivities via

$$A_b = \rho_b^o/L_o = 70.5 \ (^oK)^2 \ \text{cm/watt} \quad ,$$

$$A_c = \rho_c^o/L_o = 143 \ (^oK)^2 \ \text{cm/watt} \quad .$$

There is a considerable discrepancy between the two determinations. This is probably due to other scattering mechanisms at low temperature such as spin waves.

Magnetic superzones were quite successful in explaining the electrical resistivity anomalies. However, in the case of thermal conductivity, it is not certain that this simple approach will be valid because of inelastic scattering. On the other hand, it will be instructive to see the effects of superzones if elastic scattering is naïvely assumed. From Equations 2.56 and 2.58 the thermal conductivity is given by

$$K_{ii} = (L_o T e^2/4\pi^3\hbar) \int_{E_F} \tau v_i \, d\ell_i \quad , \tag{5.14}$$

and

$$T/K_b = A_b \quad , \tag{5.12a}$$

$$T/K_c = A_c \quad . \tag{5.12b}$$

Since electron-impurity scattering is elastic, the Wiedemann-Franz law holds and

$$K_b = L_o T/\rho_b^o \quad , \tag{5.13a}$$

$$K_c = L_o T/\rho_c^o \quad , \tag{5.13b}$$

where ρ_b^o and ρ_c^o are the residual resistivities. Thus, the constant A_b and A_c are related to the residual resistivities via

$$A_b = \rho_b^o/L_o = 70.5\ (^oK)^2\ \text{cm/watt} \quad ,$$

$$A_c = \rho_c^o/L_o = 143\ (^oK)^2\ \text{cm/watt} \quad .$$

There is a considerable discrepancy between the two determinations. This is probably due to other scattering mechanisms at low temperature such as spin waves.

Magnetic superzones were quite successful in explaining the electrical resistivity anomalies. However, in the case of thermal conductivity, it is not certain that this simple approach will be valid because of inelastic scattering. On the other hand, it will be instructive to see the effects of superzones if elastic scattering is naïvely assumed. From Equations 2.56 and 2.58 the thermal conductivity is given by

$$K_{ii} = (L_o T e^2/4\pi^3\hbar) \int_{E_F} \tau v_i \, d\ell_i \quad , \tag{5.14}$$

and

$$K_{zz} \propto \int_{E_F} \tau v_z \, d\mathcal{A}_z \quad , \tag{5.15a}$$

$$K_{xx} \propto \int_{E_F} \tau v_x \, d\mathcal{A}_x \quad . \tag{5.15b}$$

At the Néel temperature large portions of the Fermi surface are destroyed in the z direction, while in the x direction there is little loss in the projected area (cf. Figure 4). Hence, as the temperature decreases through the Néel temperature, K_{zz} will decrease sharply, while K_{xx} will remain unchanged. Experimentally, K_c decreases sharply below the transition and thus the superzone theory does predict qualitatively the correct behavior.

Just as in the case of the electrical resistivity, superzones do not affect K_a and K_b. The anomalous change in slope at the Néel temperature for ρ_a and ρ_b is due to the change in order. Now ρ_b decreases linearly with temperature and by the Wiedemann-Franz law K_b should be constant; however, at the Néel temperature ρ_b decreases very rapidly and hence K_b should increase. Although experimentally K_b is not constant above the Néel temperature, this argument does predict the correct increase in K_b below the transition.

It is interesting to note that ρ_c goes through a smooth maximum at $45^{\circ}K$ and that K_c goes through a smooth minimum at $40^{\circ}K$. Even though the scattering in this temperature range is inelastic the thermal conductivity and the electrical resistivity are still intimately related.

The observed Seebeck coefficients of thulium are very anomalous. Equations 2.37 predict a phonon drag peak between 16 and $32^{\circ}K$ for thulium, however, S_b and S_a exhibit some sort of drag peak around $45^{\circ}K$. This

suggests that magnon drag effects may be important.

The effect of magnetic superzones on the Seebeck coefficients has been considered by Mackintosh (33). He predicted (cf. Equations 3.38) that S_c will decrease and S_a will increase below the Néel temperature. This does not agree with the experimental results. Both erbium and thulium have the same type of magnetic structure transitions at their respective Néel temperatures, however, there is no similarity between their respective Seebeck coefficients. Obviously the Seebeck coefficients are so sensitive, to the detailed scattering mechanisms at the transition temperature, that a very accurate theoretical analysis will be needed to understand these phenomena.

To further complicate matters, thulium has two carriers (the s and d conduction electrons) and also there is the possibility of Umklapp processes for both magnon and phonon drag effects. A starting point, towards the understanding of the Seebeck coefficients for thulium, might be an experimental and theoretical study of the single crystal Seebeck coefficients of lutetium.

The final points to be discussed are the anomalies observed in K_c and S_c around $30^{\circ}K$ and the squaring off of the magnetic structure. There is no observed anomaly in ρ_c around $30^{\circ}K$ for thulium, however, for erbium the squaring off of the magnetic structure is reflected in its c-axis resistivity. This suggests in thulium the squaring process might be gradual. Furthermore, neutron diffraction measurements indicate a graduate appearance of the higher order harmonics around $38^{\circ}K$. Also, Elliott (48,49) suggests that a gradual squaring process in thulium is energetically

possible. Magnetic moment measurements and a careful neutron diffraction study in the 25 to 40^{o}K range might resolve this issue.

VI. BIBLIOGRAPHY

1. Nigh, H. E., S. Legvold, and F. H. Spedding, Phys. Rev., 132, 1092 (1963).

2. Green, R. W., S. Legvold, and F. H. Spedding, Phys. Rev., 122, 827 (1961).

3. Strandburg, D. L., S. Legvold, and F. H. Spedding, Phys. Rev., 127, 2046 (1962).

4. Hall, P. M., S. Legvold, and F. H. Spedding, Phys. Rev., 117, 971 (1960).

5. Hegland, D. E., S. Legvold, and F. H. Spedding, Phys. Rev., 131, 158 (1963).

6. Sill, L. R. and S. Legvold, Phys. Rev., 137, A1139 (1965).

7. Colvin, R. V., S. Legvold, and F. H. Spedding, Phys. Rev., 120, 741 (1960).

8. Born, H. J., S. Legvold, and F. H. Spedding, J. Appl. Phys., 32, 2543 (1961).

9. Jolliffe, B. W., R. P. Tye, and R. W. Powell, J. Less-Common Metals, 11, 388 (1966).

10. Aliev, N. G. and N. V. Volkenshteĭn, Soviet Phys. JETP, 22, 997 (1966).

11. Jennings, L. D., E. Hill, and F. H. Spedding, J. Chem. Phys., 34, 2082 (1961).

12. Lounasmaa, O. V. and L. J. Sundström, Phys. Rev., 150, 399 (1966).

13. Rhodes, B. L., S. Legvold, and F. H. Spedding, Phys. Rev., 109, 1547 (1958).

14. Néel, L., Z. Electrochem., 45, 379 (1939).

15. Néel, L., Compt. Rend., 206, 49 (1938).

16. Davis, D. D. and R. M. Bozorth, Phys. Rev., 118, 1543 (1960).

17. Jelinek, F. J., E. D. Hill, and B. C. Gerstein, J. Phys. Chem. Solids, 26, 1475 (1965).

18. Koehler, W. C., J. W. Cable, E. O. Wollan, and M. K. Wilkinson, J. Appl. Phys., 33, 1124 (1962).

19. Koehler, W. C., J. W. Cable, E. O. Wollan, and M. K. Wilkinson, Phys. Rev., 126, 1672 (1962).

20. Koehler, W. C., J. Appl. Phys., 36, 1078 (1965).

21. Houston, W. V., Z. Physik, 48, 449 (1928).

22. Bloch, F., Z. Physik, 52, 555 (1928).

23. Ziman, J. M., Electrons and phonons, London, England, Oxford University Press, 1960.

24. Ziman, J. M., Principle of the theory of solids, Cambridge, England, Cambridge University Press, 1964.

25. Boas, W. and J. K. Mackenzie, Prog. Metal Phys., 2, 90 (1950).

26. Elliott, R. J. and F. A. Wedgewood, Proc. Phys. Soc., 81, 846 (1963).

27. Freeman, A. J., J. O. Dimmock, and R. E. Watson, Phys. Rev. Letters, 16, 94 (1966).

28. Mackintosh, A. R., Phys. Letters, 4, 140 (1963).

29. Dekker, A. J., J. Appl. Phys., 36, 906 (1965).

30. MacDonald, D. K. C., Thermoelectricity: an introduction to the principles, New York, New York, John Wiley and Sons, Inc., 1962.

31. Bailyn, M., Phys. Rev., 126, 2040 (1962).

32. Blatt, F. J., D. J. Flood, V. Rowe, P. A. Schroeder, and J. E. Cox, Phys. Rev. Letters, 18, 395 (1967).

33. Sill, L. R., Seebeck effect in heavy rare earth single crystals, unpublished Ph.D. thesis, Ames, Iowa, Library, Iowa State University of Science and Technology, 1964.

34. Peierls, R., Ann. Phys., Ser. 5, 3, 1055 (1929).

35. Stern, H., J. Phys. Chem. Solids, 26, 153 (1965).

36. Kasuya, T., Prog. Theor. Phys., 22, 227 (1959).

37. Spedding, F. H. and J. E. Powell, J. Metals, 6, 1131 (1954).

38. Nigh, H. E., J. Appl. Phys., 34, 3323 (1963).

39. Powell, R. L., M. D. Bunch, and R. J. Corruccini, Cryogenics, 1, 139 (1961).

40. Rhyne, J. J., Magnetostriction of dysprosium, erbium, and terbium single crystals, unpublished Ph.D. thesis, Ames, Iowa, Library, Iowa State University of Science and Technology, 1965.

41. Stromberg, T. F., The superconducting properties of high purity niobium, unpublished Ph.D. thesis, Ames, Iowa, Library, Iowa State University of Science and Technology, 1965.

42. Borelius, G., W. H. Kesom, C. H. Johansson, and J. O. Linde, Proc. K. Akad. Amst., 35, 10 (1932).

43. Christian, J. W., J. P. Jan, W. B. Pearson, and I. M. Templeton, Proc. Roy. Soc. (London), A245, 213 (1958).

44. Trego, A. L., Antiferromagnetism in dilute chromium alloys, unpublished Ph.D. thesis, Ames, Iowa, Library, Iowa State University of Science and Technology, 1965.

45. Boys, D. W., Thermal conductivity of some heavy rare earth single crystals, unpublished Ph.D. thesis, Ames, Iowa, Library, Iowa State University of Science and Technology, [to be submitted 1967].

46. Alstad, J. K., R. V. Colvin, and S. Legvold, Phys. Rev., 123, 418 (1961).

47. Keeton, S. C. and T. L. Loucks, Antiferromagnetism and the Fermi surface in some heavy rare earths, Phys. Rev. Letters, [to be published ca. 1967].

48. Elliott, R. J., Phys. Rev., 124, 346 (1961).

49. Elliott, R. J., Theory of magnetism in the rare earths, in Rado, G. T. and H. Suhl, eds., Magnetism, Vol. 2A, pp. 385-424, New York, New York, Academic Press, 1965.

VII. ACKNOWLEDGEMENTS

The author would like to express his thanks to his major professor and friend, Dr. Sam Legvold, for suggesting this problem and for his interest, encouragement, and help during this study.

Thanks are extended to Dr. S. Liu, to Dr. C. A. Swenson, and to Dr. D. K. Finnemore for many valuable discussions, and also to Mr. B. J. Beaudry for his skillful arc-melting of the thulium buttons, and to Dr. D. T. Peterson for discussions concerning twins.

Grateful appreciation is expressed to Mr. D. W. Boys for the use of his thermal conductivity apparatus and to Mr. D. B. Richards for help in the early attempts to grow thulium single crystals.

It is a pleasure to acknowledge Dr. J. J. Rhyne, Dr. L. R. Sill, Dr. A. L. Trego, Dr. L. Muhlestein, Dr. R. Lee, Dr. S. Keeton, Mr. C. M. Cornforth and Mr. W. Nellis for numerous helpful discussions.

Thanks are extended to Mr. W. Sylvester and Mr. R. Brown for aid in constructing the experimental apparatus and to Mr. G. Erskine for his assistance in maintaining the equipment and in processing data.

The author would like to publicly express his gratitude to his wife, Judy, for her encouragement, patience and good humor during his graduate career and for the typing of the rough draft.

VIII. APPENDIX

A. Sample Dimensions

Sample dimensions of all the samples used in this study are listed in Table 1. The average cross-sectional areas are also listed. Samples $Tm(a_1)$, $Tm(b_1)$, and $Tm(c_1)$ were used for the electrical resistivity and thermoelectric power measurements, while samples of larger cross-section $Tm(b_2)$ and $Tm(c_2)$ were needed for the thermal conductivity measurements.

Table 1. Sample dimensions and cross-sectional areas

Sample	Length (cm)	Height (mm)	Width (mm)	Cross-sectional Area $(mm)^2$
$Tm(a_1)$	0.716	1.074	1.259	1.352
$Tm(b_1)$	0.770	1.190	1.311	1.559
$Tm(c_1)$	0.791	0.801	1.016	0.814
$Tm(b_2)$	0.723	1.224	1.250	1.532
$Tm(c_2)$	0.724	1.166	1.450	1.690

B. Sample Impurities

The gaseous impurities were determined by vacuum fusion analysis and the other impurities were determined by semi-quantitative analysis. The analyses were done on the same grains from which the crystals were cut. The impurities are listed in Table 2. All impurities are recorded in ppm by weight. Lanthanum, cerium, neodymium, samarium, europium, gadolinium, and terbium were not detected.

Table 2. Sample impurities

Impurities	$Tm(a_1)$	$Tm(b_{1,2})$	$Tm(c_{1,2})$
Al	< 60	< 60	< 60
Ca	< 20	< 20	< 20
Cr	< 20	< 20	< 20

Table 2. (Continued)

Impurities	$Tm(a_1)$	$Tm(b_{1,2})$	$Tm(c_{1,2})$
Fe	< 50	< 50	< 50
Mg	< 10	< 10	< 10
Ni	< 50	< 50	< 50
Si	< 60	< 60	< 60
Er	< 30	< 30	< 30
Yb	< 10	< 10	< 10
Lu	< 200	< 200	< 200
Ho	< 200	< 200	< 200
Y	< 200	< 200	< 200
Mn		T	FT
Cu	T		T
W			FT
Dy	T	FT	T
Y	FT		
O_2	83	61	100
N_2			3
H_2	5	1	4

The residual resistivity ($\rho_{4.2}$) and the resistance ratio ($\rho_{300}/\rho_{4.2}$) are also indicative of sample purity. In Table 3, the residual resistivity and resistance ratios are listed for all the samples. The residual resistivities are in units of $\mu\,\Omega$-cm.

Table 3. Residual resistivities and resistance ratios

Sample	Residual Resistivity	Resistance Ratios
$Tm(a_1)$	2.39	38.1
$Tm(b_{1,2})$	1.73	51.0
$Tm(c_{1,2})$	3.65	12.9

C. Tabulation of the Electrical Resistivity Data

The resistivities are recorded in units of μΩ-cm and the temperatures are in ^{o}K.

Table 4. Experimental data for the a-axis crystal

ρ	T	ρ	T	ρ	T
2.388	1.3	2.388	3.9	2.516	11.0
2.388	1.8	2.388	4.2	2.590	12.0
2.387	2.1	2.388	5.0	2.701	13.0
2.388	2.4	2.390	6.0	2.834	14.0
2.387	2.7	2.396	7.0	3.025	15.0
2.388	3.0	2.407	8.0	3.200	16.0
2.388	3.3	2.427	9.0	3.718	18.0
2.388	3.6	2.462	10.0	4.452	20.1
5.351	22.2	23.29	45.9	40.02	77.8
5.901	24.0	24.08	46.7	40.66	79.4
7.387	26.0	26.31	49.1	42.06	83.9
8.502	28.0	27.31	50.1	44.18	91.5
10.29	30.3	28.77	51.7	46.35	99.5
10.08	30.4	29.95	53.0	50.34	115.0
11.71	32.3	31.41	54.6	54.24	130.8
13.01	33.8	33.18	57.0	57.76	145.7
14.65	36.0	33.68	58.2	61.20	160.5
15.56	37.1	34.36	60.0	66.02	181.9
16.40	38.1	34.79	61.0	70.31	201.5
17.82	39.8	35.54	63.4	74.54	221.2
18.17	40.3	36.63	66.6	78.55	240.8
19.35	41.6	37.41	69.0	82.95	261.4
20.71	43.1	38.41	72.1	87.18	280.9
22.05	44.5	39.52	75.7	91.19	299.6

Table 5. Experimental data for the b-axis crystals

ρ	T	ρ	T	ρ	T
1.730	2.7	1.730	4.2	1.761	9.0
1.730	3.0	1.731	5.0	1.798	10.0
1.731	3.3	1.733	6.0	1.902	12.0
1.730	3.6	1.736	7.0	2.114	14.0
1.729	3.9	1.746	8.0	2.461	16.0
2.949	18.1	15.98	39.3	42.03	91.1
3.633	20.2	18.41	42.2	44.66	101.1
3.688	20.3	21.97	46.3	49.44	120.3
4.453	22.2	25.53	50.1	54.42	141.4
5.522	24.5	29.07	54.0	58.76	160.5
6.492	26.2	31.11	56.5	63.25	180.7
6.891	26.8	31.92	58.0	67.54	200.6
7.703	28.3	32.76	60.3	71.91	221.1
8.442	29.3	34.44	65.3	76.20	241.6
10.35	32.1	36.23	70.9	80.25	261.1
12.81	35.4	37.97	76.6	84.34	280.9
13.57	36.3	39.72	82.7	88.12	298.9

Table 6. Experimental data for the c-axis crystal

ρ	T	ρ	T	ρ	T
3.641	1.4	3.647	4.2	4.413	13.0
3.643	1.7	3.649	5.0	4.729	14.0
3.642	2.1	3.657	6.0	5.102	15.0
3.644	2.4	3.677	7.0	5.558	16.0
3.644	2.7	3.708	8.0	6.093	17.0
3.645	3.0	3.764	9.0	6.715	18.0
3.645	3.3	3.848	10.0	7.416	19.0
3.645	3.6	3.981	11.0	8.218	20.0
3.646	4.0	4.161	12.0	8.389	20.3
9.121	21.0	25.73	43.3	19.06	68.6
10.01	22.0	25.81	44.1	19.38	71.1

Table 6. (Continued)

ρ	T	ρ	T	ρ	T
10.88	22.7	25.85	45.4	19.68	73.6
10.96	23.0	25.72	47.1	19.96	75.8
11.93	24.0	25.40	48.7	20.23	77.9
12.91	24.7	24.92	50.0	20.51	80.1
12.93	25.0	24.35	51.2	21.09	84.9
13.94	26.0	23.69	52.3	21.98	92.1
14.89	26.7	22.32	53.9	22.92	100.1
17.53	29.4	21.24	54.9	23.88	108.3
19.37	31.1	20.86	55.2	25.33	120.8
21.61	33.6	20.29	55.7	26.87	134.3
22.80	35.2	19.90	56.0	28.17	145.6
23.60	36.3	18.60	56.8	29.91	160.6
23.87	37.3	17.80	57.5	31.92	177.8
24.02	37.6	17.81	57.9	33.93	195.0
24.57	38.9	17.92	59.4	35.91	211.7
25.02	40.1	18.21	61.9	38.10	229.9
25.37	41.4	18.48	64.2	40.52	249.6
25.53	42.1	18.73	66.1	43.62	274.3
				47.05	300.7

D. Tabulation of the Seebeck Coefficient Data

The Seebeck coefficients are recorded in units of μvolts/^{o}K and the temperatures are in ^{o}K.

Table 7. Experimental data for the a-axis crystal

S	T	S	T	S	T
-0.369	7.6	-1.70	38.4	-0.984	86.3
-0.392	8.5	-1.76	40.9	-0.977	91.5
-0.406	9.5	-1.82	43.4	-0.965	96.4
-0.421	10.5	-1.83	46.0	-0.942	101.5

Table 7. (Continued)

S	T	S	T	S	T
-0.438	11.8	-1.71	48.4	-0.878	111.4
-0.474	12.8	-1.54	50.9	-0.792	121.4
-0.512	13.8	-1.25	53.5	-0.674	131.0
-0.556	14.9	-0.898	56.1	-0.547	141.0
-0.612	15.8	-0.723	57.5	-0.423	150.8
-0.659	16.8	-0.702	58.9	-0.263	164.7
-0.691	17.8	-0.758	61.0	-0.123	175.7
-0.736	18.8	-0.762	62.7	0.048	190.3
-0.843	21.6	-0.818	64.0	0.223	205.9
-0.901	23.0	-0.837	66.8	0.399	220.7
-0.975	25.0	-0.887	70.4	0.611	242.0
-1.08	27.3	-0.934	74.7	0.808	261.1
-1.17	28.9	-0.963	78.4	1.02	282.0
-1.26	31.2	-0.896	71.6	1.22	300.3
-1.43	33.8	-0.946	76.5		
-1.57	36.3	-0.971	81.4		

Table 8. Experimental data for the b-axis crystal

S	T	S	T	S	T
-0.053	7.3	-1.15	31.6	-0.935	80.9
-0.057	8.6	-1.42	35.0	-0.946	91.5
-0.064	9.5	-1.52	37.0	-0.898	101.4
-0.067	10.5	-1.53	38.1	-0.760	120.7
-0.083	11.5	-1.71	42.3	-0.529	140.1
-0.104	12.5	-1.72	45.4	-0.273	159.5
-0.182	14.5	-1.67	47.5	-0.020	179.9
-0.303	16.6	-1.48	50.6	0.201	199.8
-0.435	18.5	-1.15	53.7	0.451	219.8
-0.595	20.7	-0.894	55.8	0.707	240.9
-0.597	21.2	-0.662	57.5	0.888	261.2
-0.744	23.7	-0.665	59.8	1.04	281.5

Table 8. (Continued)

S	T	S	T	S	T
-0.830	25.7	-0.762	63.7	1.24	300.5
-0.912	26.8	-0.824	68.6		
-1.03	29.7	-0.867	74.2		

Table 9. Experimental data for the c-axis crystal

S	T	S	T	S	T
0.236	7.3	-0.072	11.7	-1.01	20.7
0.233	7.8	-0.156	12.6	-1.02	21.3
0.213	8.8	-0.284	13.6	-1.15	22.7
0.174	9.7	-0.463	15.1	-1.39	25.0
0.150	10.2	-0.634	16.7	-1.62	26.7
0.017	10.7	-0.872	19.2	-1.85	28.7
-2.09	30.6	-1.48	56.7	-1.91	121.2
-2.24	32.8	-1.53	57.1	-1.78	130.3
-1.95	34.9	-1.65	58.8	-1.60	140.5
-1.89	36.9	-1.70	59.1	-1.39	150.5
-1.90	38.8	-1.81	61.9	-1.19	160.5
-1.90	40.8	-1.95	65.5	-0.980	170.0
-1.91	42.9	-2.04	70.7	-0.787	180.6
-1.90	45.0	-2.08	75.9	-0.565	190.6
-1.75	48.9	-2.13	79.1	-0.337	200.4
-1.64	50.8	-2.14	85.9	0.012	216.5
-1.53	52.1	-2.15	90.9	0.360	231.2
-1.45	53.7	-2.17	91.0	0.733	246.5
-1.46	54.7	-2.12	100.8	1.09	261.9
-1.45	55.6	-2.02	111.3	1.59	281.8

E. Tabulation of the Thermal Conductivity Data

The thermal conductivities are in units of watts/cm-^{o}K and the temperatures are in ^{o}K.

Table 10. Experimental data for the b-axis crystal

K	T	K	T	K	T
0.133	5.1	0.209	8.0	0.238	10.0
0.195	7.5	0.223	9.1	0.245	11.1
0.247	12.2	0.127	33.4	0.102	71.8
0.246	13.4	0.121	35.7	0.105	75.9
0.242	14.7	0.113	37.5	0.111	101.2
0.230	16.1	0.108	40.1	0.115	120.9
0.221	17.6	0.108	43.3	0.121	141.1
0.209	18.6	0.100	47.1	0.128	161.1
0.204	19.6	0.095	50.6	0.132	181.1
0.192	20.9	0.092	53.5	0.133	200.9
0.194	21.5	0.090	55.8	0.136	220.8
0.181	22.7	0.093	56.5	0.137	240.9
0.180	23.6	0.091	57.8	0.138	260.8
0.165	25.5	0.092	59.2	0.141	280.8
0.146	28.4	0.097	62.8	0.143	298.5
0.136	30.7	0.096	66.8		

Table 11. Experimental data for the c-axis crystal

K	T	K	T	K	T
0.132	5.4	0.197	13.7	0.123	24.7
0.181	7.6	0.179	15.7	0.118	25.5
0.195	8.8	0.159	17.8	0.116	26.8
0.203	9.7	0.149	19.4	0.110	28.5
0.209	10.7	0.136	21.5	0.107	30.0
0.207	11.7	0.132	21.7	0.107	31.4
0.206	12.6	0.128	23.6	0.105	32.4

Table 11. (Continued)

K	T	K	T	K	T
0.105	33.2	0.158	57.4	0.220	140.7
0.104	34.2	0.163	58.5	0.226	160.6
0.103	36.1	0.163	59.6	0.231	180.9
0.104	37.9	0.160	61.0	0.232	201.0
0.103	39.7	0.166	62.4	0.239	221.1
0.104	41.7	0.170	66.6	0.239	240.9
0.107	44.4	0.176	70.5	0.240	261.0
0.112	47.3	0.184	80.6	0.241	280.8
0.121	50.7	0.194	90.7	0.241	298.6
0.132	53.6	0.202	100.7		
0.144	56.1	0.211	121.0		

F. Discussion of Errors

The electrical resistivity (cf. Equation 3.1) is computed experimentally from

$$\rho = (V/I)A/L \quad . \tag{8.1}$$

The absolute fractional error is

$$\delta\rho/\rho = [(\delta V/V)^2 + (\delta m/I)^2 + (\delta L/L)^2 + (\delta A/A)^2]^{1/2} \quad . \tag{8.2}$$

The relative error is determined by the first two terms. The current was stable to within 0.02% over the period of measurement and was measured for both the forward and reverse directions. The potential, V, was measured to within 0.02% for low voltages (resistivity is small at low temperatures) and to within 0.002% for high voltages (resistivity is large at high temperatures). Thus, the maximum relative error is 0.04%. The current was reversed to eliminate the thermal emfs in the voltage circuit, and the temperature control was sufficiently stable such that no drifting was

detectable in either V or I. The absolute error is determined by the last two terms in Equation 8.2. The distance between voltage probes, L, was measured to within 1%, and the cross-sectional area was measured to within 4%. Therefore, the absolute error is approximately 4.5%.

Thermocouples were used to measure the absolute temperature of the sample for all the measurements made in this study. The absolute error in the temperature was $\pm 0.1^{\circ}K$ for the 4.2 to $25^{\circ}K$ range and $\pm 0.5^{\circ}K$ for the 25 to $300^{\circ}K$ range.

The same method for both the thermoelectric power and thermal conductivity was used to measure the temperature gradient. The temperature gradient is computed by

$$\Delta T = \Delta E_{AC}/S_{AC} \quad , \tag{8.3}$$

and the absolute fractional error is computed from

$$\delta(\Delta T)/T = [(\delta(\Delta E_{AC})/\Delta E_{AC})^2 + (\delta S_{AC}/S_{AC})^2]^{1/2} \quad . \tag{8.4}$$

ΔE_{AC} was measured with a Dauphinee comparator and, due to charge decay in the resistive-capacitive networks, the comparator always measured 0.5% low. As mentioned earlier in Section III, the sensitivity, S_{AC}, was determined by differentiating the thermocouple emf versus T curves. S_{AC} is smallest for both thermocouples (Cu-Con, Cu-AuFe) in the 20 to $30^{\circ}K$ range, and the maximum error is estimated to be approximately 1%. Another serious error is thermocouple mismatch (due to inhomogenities in the wires). This mismatch was measured (cf. Section III) to within approximately 1%. Since the thermocouples were soldered to the ends of the sample with indium solder, there could exist a small temperature gradient across the junction. There

is no practical way to estimate this effect. The maximum error in ΔT is estimated to be approximately 2% at low temperatures and reduces to about 1% at high temperatures.

The relative Seebeck coefficient (cf. Equation 3.9) is determined from

$$S_{AX} = \Delta V_{AX}/\Delta T \quad , \tag{8.5}$$

and the fractional error is computed by

$$\delta S_{AX}/S_{AX} = [(\delta(\Delta V_{AX})/\Delta V_{AX})^2 + (\delta(\Delta T)/\Delta T)^2]^{1/2} \quad . \tag{8.6}$$

At low temperatures ($T < 10^{o}K$) ΔV_{AX} was on the order of 0.1 microvolts and it was difficult to estimate the error because of thermals in the Seebeck circuit. In Section III a method was described to partially eliminate these thermals. The error in ΔV_{AX} was estimated to be about 10% below $10^{o}K$. Above $10^{o}K$ ΔV_{AX} increased rapidly to several microvolts and thus the error dropped to less than 1%. The absolute Seebeck coefficient is determined by

$$S_X = S_A - S_{AX}$$

and the errors discussed above will also be present in the calibration run for S_A. The absolute error is estimated to be 10% for $T < 10^{o}K$ and 5% for $10^{o}K < T < 30^{o}K$. Above $30^{o}K$ the error gradually decreases to 2% and remains constant up to room temperature. From the lack of scatter in the data, the relative error in S_X is estimated to be within 0.03 microvolts/^{o}K.

The thermal conductivity (cf. Equation 3.11) is computed from

$$K = (Q/\Delta T)(L/A) \quad , \tag{8.7}$$

and the fractional error is given by

$$\delta K/K = [(\delta Q/Q)^2 + (\delta(\Delta T)/\Delta T)^2 + (\delta L/L)^2 + (\delta A/A)^2]^{1/2} \quad . \qquad (8.8)$$

The relative error is determined by the first two terms. Now $Q = P-P_0$, where P is the power produced by the joule heating of the gradient heater and P_0 is the power lost due to radiation, and conduction through the thermocouple and heater leads to the "hot" end of the sample. The error in P was estimated to be about 0.5%. Radiation losses were negligible below $60^{\circ}K$ and become significant above $150^{\circ}K$. The conduction losses were estimated to be about 2% below $60^{\circ}K$ and were neglected. The technique used for radiation corrections is described by Boys (45) and the error in the measurement of P_0 is estimated to be about 2-3%. Thus, the relative error is approximately 4%. The absolute error is determined by all the terms in Equation 8.8. The length of the sample, L, was measured to within 1% and the cross-sectional area was within 4%. Thus, the absolute error is within 6 to 8%.